Article

Immunity

In Vivo Killing Capacity of Cytotoxic T Cells Is Limited and Involves Dynamic Interactions and T Cell Cooperativity

Graphical Abstract

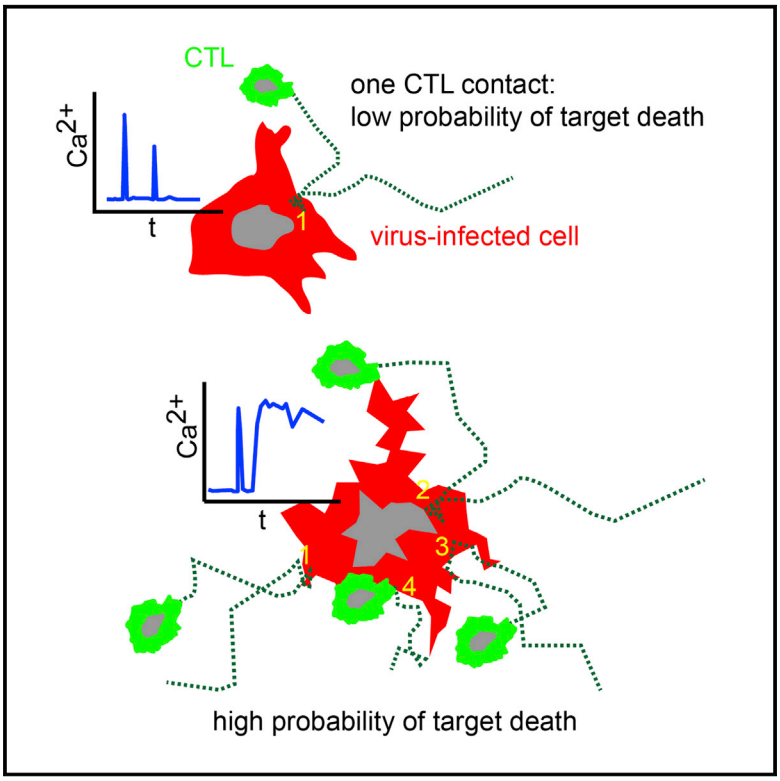

Authors

Stephan Halle, Kirsten Anja Keyser, Felix Rolf Stahl, ..., Gerd Sutter, Martin Messerle, Reinhold Förster

Correspondence

halle.stephan@mh-hannover.de (S.H.), foerster.reinhold@mh-hannover.de (R.F.)

In Brief

According to in vitro assays, T cells are thought to kill rapidly and efficiently. Using two-photon microscopy, Forster and colleagues have found that killing capacities of single cytotoxic T lymphocytes (CTLs) in vivo are heterogeneous and limited. Quantification of target-cell-death probabilities identified efficient cooperative killing when multiple CTLs attacked a virus-infected cell.

Highlights

- Two-photon imaging indicates that CTLs kill 2–16 virus-infected cells per day
- CTLs form kinapses rather than stable synapses when killing virus-infected cells
- Some CTL contacts trigger long-lasting calcium fluxes in virus-infected cells
- CTLs can cooperate during killing of virus-infected cells

Halle et al., 2016, Immunity *44*, 233–245
February 16, 2016
http://dx.doi.org/10.1016/j.immuni.2016.01.010

CellPress

Immunity
Article

In Vivo Killing Capacity of Cytotoxic T Cells Is Limited and Involves Dynamic Interactions and T Cell Cooperativity

Stephan Halle,[1,*] Kirsten Anja Keyser,[2] Felix Rolf Stahl,[1,10] Andreas Busche,[2,11] Anja Marquardt,[2,12] Xiang Zheng,[1] Melanie Galla,[3] Vigo Heissmeyer,[4,5] Katrin Heller,[1] Jasmin Boelter,[1] Karen Wagner,[2] Yvonne Bischoff,[1] Rieke Martens,[1] Asolina Braun,[1,13] Kathrin Werth,[1] Alexey Uvarovskii,[6] Harald Kempf,[6] Michael Meyer-Hermann,[6,7] Ramon Arens,[8] Melanie Kremer,[9] Gerd Sutter,[9] Martin Messerle,[2] and Reinhold Förster[1,*]
[1]Institute of Immunology, Hannover Medical School, 30625 Hannover, Germany
[2]Institute of Virology, Hannover Medical School, 30625 Hannover, Germany
[3]Institute of Experimental Hematology, Hannover Medical School, 30625 Hannover, Germany
[4]Institute for Immunology, Ludwig-Maximilians-Universität München, 80336 München, Germany
[5]Institute of Molecular Immunology, Helmholtz Zentrum München, 81377 München, Germany
[6]Department of Systems Immunology and Braunschweig Integrated Centre of Systems Biology, Helmholtz Centre for Infection Research, 38124 Braunschweig, Germany
[7]Institute for Biochemistry, Biotechnology, and Bioinformatics, Technische Universität Braunschweig, 38124 Braunschweig, Germany
[8]Department of Immunohematology and Blood Transfusion, Leiden University Medical Center, 2333 ZA Leiden, the Netherlands
[9]Institute for Infectious Diseases and Zoonoses, Ludwig-Maximilians-Universität München, 80539 München, Germany
[10]Present address: Institute of Clinical Chemistry and Laboratory Medicine, University Medical Center Hamburg-Eppendorf, 20246 Hamburg, Germany
[11]Present address: Merck Animal Health, Burgwedel Biotech GmbH, 30938 Burgwedel, Germany
[12]Present address: Octapharma Produktionsgesellschaft Deutschland mbH, 31832 Springe, Germany
[13]Present address: Institute of Microbiology and Immunology, University of Melbourne, Melbourne, VIC 3010, Australia
*Correspondence: halle.stephan@mh-hannover.de (S.H.), foerster.reinhold@mh-hannover.de (R.F.)
http://dx.doi.org/10.1016/j.immuni.2016.01.010

SUMMARY

According to in vitro assays, T cells are thought to kill rapidly and efficiently, but the efficacy and dynamics of cytotoxic T lymphocyte (CTL)-mediated killing of virus-infected cells in vivo remains elusive. We used two-photon microscopy to quantify CTL-mediated killing in mice infected with herpesviruses or poxviruses. On average, one CTL killed 2–16 virus-infected cells per day as determined by real-time imaging and by mathematical modeling. In contrast, upon virus-induced MHC class I downmodulation, CTLs failed to destroy their targets. During killing, CTLs remained migratory and formed motile kinapses rather than static synapses with targets. Viruses encoding the calcium sensor GCaMP6s revealed strong heterogeneity in individual CTL functional capacity. Furthermore, the probability of death of infected cells increased for those contacted by more than two CTLs, indicative of CTL cooperation. Thus, direct visualization of CTLs during killing of virus-infected cells reveals crucial parameters of CD8$^+$ T cell immunity.

INTRODUCTION

CD8$^+$ cytotoxic T lymphocytes (CTLs) play an essential role in combating viral infections (Zhang and Bevan, 2011). During activation by antigen-presenting cells, CTLs integrate T cell receptor (TCR), co-stimulatory, and cytokine receptor signaling to fine-tune proliferation and differentiation and establish various effector cell subtypes characterized by the expression of different surface markers and cytokine production abilities (Marchingo et al., 2014). Together, these mechanisms allow the generation of CTL responses that can defend the host organism during primary infection and provide protective immunity against reinfection.

Primed CTLs are able to detect viral peptides restricted to major histocompatibility complex class I (MHC-I) and establish a TCR-triggered immunological synapse with their targets to secrete the content of their cytotoxic granules toward the infected cell (Dustin, 2008). The targeted secretion of several effector proteins, such as granzymes and perforin, triggers the cell-death machinery in the infected cell while leaving antigen-negative bystander cells intact (Lopez et al., 2012). Furthermore, CTLs secrete various cytokines that contribute to antiviral immunity. However, it remains unclear how important the contact-dependent killing of target cells is in relation to these indirect mechanisms of control.

The efficiency of CTL-mediated contact-dependent killing of different cell types has been studied extensively in vitro. Such studies have suggested that CTLs can rapidly, serially, and even simultaneously kill multiple target cells within minutes (Wiedemann et al., 2006). However, assays of in vitro killing have a limited capacity to reflect the situation of how CTLs sense, reach, and interact with infected cells in a three-dimensional tissue in vivo. Whereas many assays of in vitro killing involve CTLs and targets co-cultured in suspension or as cell pellets, access to infected cells is likely to be limited in the intact

tissue in which only selected cells are infected with viruses. Also, the extracellular matrix and bystander cells might exert multiple, often suppressive effects on CTL function (Zhang and Bevan, 2011). In addition, in co-culture killing assays, CTLs are brought passively together with target cells, whereas in vivo killing requires active CTL sensing and migration (Germain et al., 2012). Thus, it remains unclear how fast and how robustly virus-infected cells are killed by single CTLs in different virus-infected tissues (Elemans et al., 2014; Elemans et al., 2012; Hickman et al., 2015; Hogan et al., 2014).

In the current study, we quantified CTL killing kinetics by two-photon microscopy in mice infected with murine cytomegalovirus (MCMV) or modified vaccinia virus Ankara (MVA). To this end, we used ex vivo two-photon imaging of explanted lymph nodes and in vivo imaging of intact skin together with transgenic and natural CTLs and virus-expressed functional reporter systems. Importantly, we found that not every contact between CTLs and target cells led to a perforin-dependent Ca^{2+} flux and target-cell death. Using datasets on single-cell tracking, we estimated the average per capita killing rates (PCKRs: the number of targets killed per CTL per day) of transgenic and endogenous CTLs that kill different types of cells infected with several strains and species of viruses. In contrast to the conventional theory of "highly efficient" killing, our results consistently showed that PCKRs in vivo were overall limited to a value of about 2–16 infected cells killed per CTL per day. Furthermore, we observed that viral MHC-I immune evasion strongly reduced CTL-mediated antigen-specific contact-dependent killing in vivo. Finally, we showed that by increasing the probability of target-cell death after multiple encounters, CTLs could cooperate during killing of virus-infected cells.

RESULTS

Single-Cell Visualization Allows for Quantification of Virus-Infected Cells

To determine killing kinetics of CTLs in vivo, we infected mice with MCMV reporter strains (Marquardt et al., 2011). MCMV-2D expresses the red fluorescent protein (FP) mCherry and a secretable Gaussia luciferase, whereas MCMV-3D additionally expresses the ovalbumin (OVA)-derived SIINFEKL peptide epitope. MCMV downmodulates surface MHC-I expression in infected cells, possibly leaving CTLs incapable of recognizing their targets (Gold et al., 2004; Hansen et al., 2010; Krmpotic et al., 1999). We therefore also used MCMV-3D-ΔvRAP, which lacks m06 and m152, two viral regulators of antigen presentation (vRAP) genes interfering with MHC-I recognition (Ziegler et al., 1997), to study the effect of MHC-I downregulation on CTL effector function.

To determine MCMV tropism after subcutaneous (s.c.) footpad infection of C57BL/6 (B6) mice with MCMV-3D, we used fluorescence microscopy to detect bright-mCherry-expressing cells in the draining popliteal lymph node at days 1 and 2 after infection. All MCMV-infected cells lacked expression of CD45 and CD169 and were located below the subcapsular sinus floor on the afferent side of the lymph node, approximately 20–30 μm beneath the capsule (Figures 1A–1E). Some MCMV-infected cells expressed the fibroblast markers podoplanin (gp38) and ER-TR7-antigen, but not the cell-adhesion molecule MAdCAM (data not shown). Thus, the MCMV strains used in this study initially infect fibroblast- or pericyte-like stromal cells, but not macrophages or dendritic cells. The number of $mCherry^+$ virus-infected cells as determined by microscopy strongly correlated with the MCMV-encoded Gaussia luciferase activity (Figure 1F and data not shown). Therefore, we used the number of intact virus-infected cells to determine infected cell densities throughout this study. Taken together, different microscopy techniques allowed for a clear and unbiased quantification of the density of intact virus-infected cells in defined micro-anatomical regions.

CTLs Fail to Recognize Virus-Infected Cells Protected by Viral Immune Evasion

We tested the ability of CTLs to directly detect and kill cells infected by different variants of MCMV after adoptive transfer of TCR-transgenic, FP-expressing, SIINFEKL-K^b-specific OT-I cells into B6 recipients. These mice were immunized with SIINFEKL peptide and poly(I:C) or with OVA protein together with MVA. Both procedures induced expansion and maturation of OT-I CTLs within 4–6 days (Figures 2A and 2B). The percentage of expanded $CD44^{hi}$ OT-I CTLs present in blood reliably predicted the number of OT-I CTLs in lymph nodes 2 days later (Figure 2C), allowing the analysis of MCMV infection in mice harboring defined numbers of virus-specific CTLs.

One day after MCMV-2D infection, CTLs expectedly did not express the activation marker CD69, and ex vivo two-photon microscopy showed that CTLs failed to attach to or kill infected cells (Figures 2D and 2E; Movie S1). Upon infection with MCMV-3D, OT-I CTLs strongly upregulated the activation marker CD69 but remained highly motile and established only a few contacts with infected cells. Consequently, most MCMV-3D-infected cells remained intact, even in the presence of high numbers of activated CTLs (Figures 2D and 2F; Movie S1).

In contrast, in lymph nodes with high CTL densities, most MCMV-3D-ΔvRAP-infected cells were killed within 24 hr after infection (Figure 2G; Movie S1). Together, these findings demonstrate that viral MHC-I immune evasion protects MCMV-3D-infected cells from CTL-mediated killing and that in the absence of viral immune evasion, high CTL densities correlate with local eradication of infected cells.

Next, we characterized migration parameters of CTLs within the first 14–20 hr after infection. Compared to CTLs in mock, MCMV-2D, or MCMV-3D infection, CTLs that attacked MCMV-3D-ΔvRAP-infected cells showed significantly reduced track speeds (Figure 3A). Furthermore, CTLs showed very low motility coefficients, a measure for CTL displacement over time, according to the random-walk-hypothesis framework (Beltman et al., 2009). Also, CTL turning angles were increased during local confinement to regions with infected cells (Figures 3B–3D). These findings demonstrate that CTLs migrate at low velocities and stay confined in small tissue volumes while recognizing virus-infected cells and that viral immune evasion significantly alters CTL migration behavior and killing of virus-infected cells.

Two-Photon Microscopy Reveals that Multiple CTLs Are Needed to Robustly Kill Virus-Infected Cells

MCMV-3D-ΔvRAP-infected targets usually remained intact after contact by a single OT-I CTL (Figures S1A and S1B; Movie S1). In

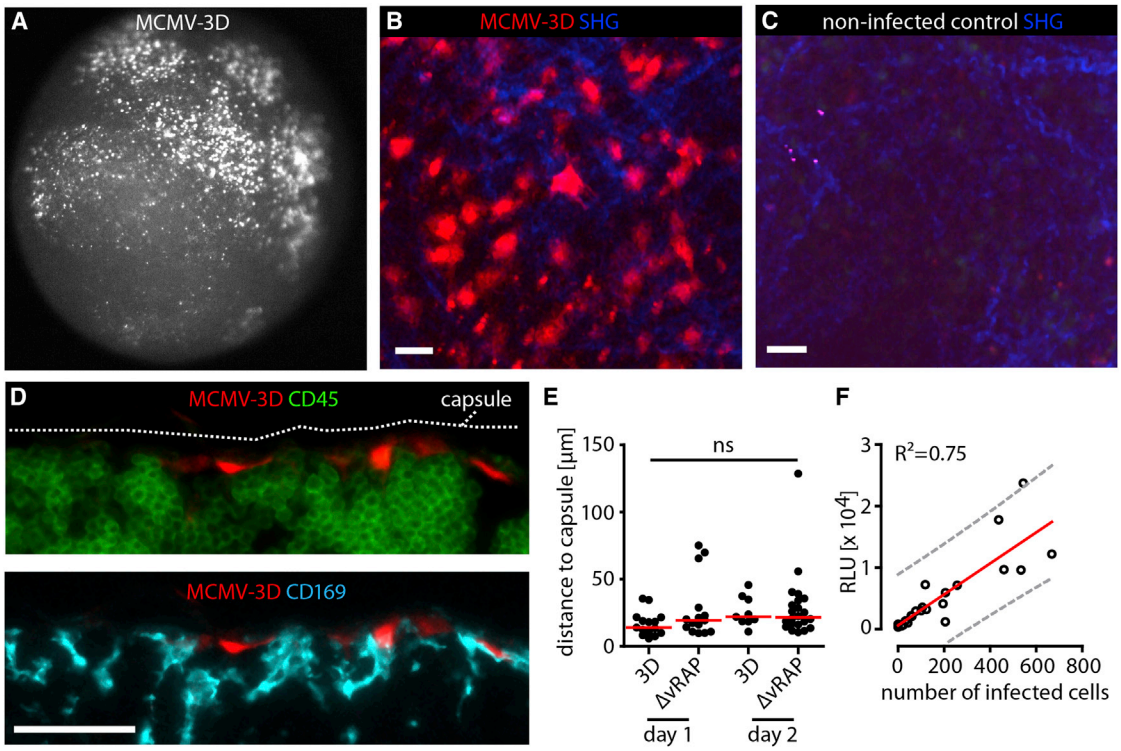

Figure 1. Single-Cell Visualization Allows for Quantification of Virus-Infected Cell Numbers

(A) Detection of mCherry$^+$ MCMV-infected cells (white) by epi-fluorescence microscopy in cortical region of the popliteal lymph node 48 hr after MCMV-3D footpad injection (10^6 plaque-forming units [PFU]) into B6 mice.

(B) One day after infection, MCMV-infected cells expressing mCherry (red) and second harmonic generation signals (SHG, blue) were observed by two-photon microscopy. Scale bar represents 20 μm.

(C) Non-infected lymph node imaged at an identical region. Scale bar represents 20 μm.

(D) MCMV-3D-infected cells (red) and counterstaining with anti-CD45 (upper panel; green) and anti-CD169 (lower panel; cyan). Pictures shown in (A)–(D) are representative of >15 experiments. Scale bar represents 20 μm.

(E) Distance of MCMV-infected cells to the lymph node capsule. Dots represent cells, and bars represent medians. Data were pooled from six mice from two independent experiments. ns, not significant.

(F) After infection with different doses of MCMV-3D, the number of MCMV-infected cells observed by microscopy was plotted against MCMV-expressed luciferase signals. The red line represents linear regression, and the 99% prediction interval is shown in gray.

contrast, when numerous CTLs interacted simultaneously or serially with MCMV-3D-ΔvRAP-infected cells, we frequently observed target cell disruption (Figure 4A; Movie S2). The killing process of the virus-infected cells took some time, and morphological changes were observed over 10–40 min, long before the target cells finally disappeared. Typically, we observed initial morphological disturbances followed by the formation of blebs and later by the shedding of larger portions, resembling apoptotic bodies, of the mCherry-labeled cell body (Figure 4A [lower panel], Figure 4B).

The cognate interaction between CTLs and their targets rarely led to stable synapses with complete arrest of CTLs. Instead, while contacting their targets, CTLs remained motile with an instantaneous velocity of 2–4 μm/min for periods of approximately 10–15 min (Figure 4C) before regaining velocity. This type of interaction between targets and CTLs resembled the formation of migratory "kinapses" observed between T cells and dendritic cells presenting antigen with intermediate or low affinity during T cell priming (Dustin, 2008). Throughout the manuscript, we will use the term "kinapse" to describe this type of migratory interaction between CTLs and virus-infected cells during target-cell killing.

Direct observation of CTL-target-cell interaction behavior and quantification of target-cell fate revealed that killed virus-infected cells experienced a median of 3.5 distinct CTL contacts, whereas surviving cells were rarely targeted (0 median contacts; Figure 4D). Killed targets encountered a cumulative median contact time of 50 min (Figure 4E). Individual contacts between CTLs and surviving targets lasted 8.5 min (Figure 4F), and individual contacts between CTLs and killed targets lasted for approximately 9.0 min (median; Figure 4F). These observations indicate that successful killing of infected cells is not simply determined by the duration of individual CTL contacts.

When comparing the different MCMV strains, we observed that 1% and 8% of CTLs established contacts with MCMV-2D- and MCMV-3D-infected cells, respectively, whereas 38% of the CTLs contacted MCMV-3D-ΔvRAP infected cells (Figures 4G and 4H). Furthermore, we found that virus-infected cells were usually disrupted within 20–60 min (but rarely within 10 min) after the first observed CTL contact (Figure 4I). Together, these

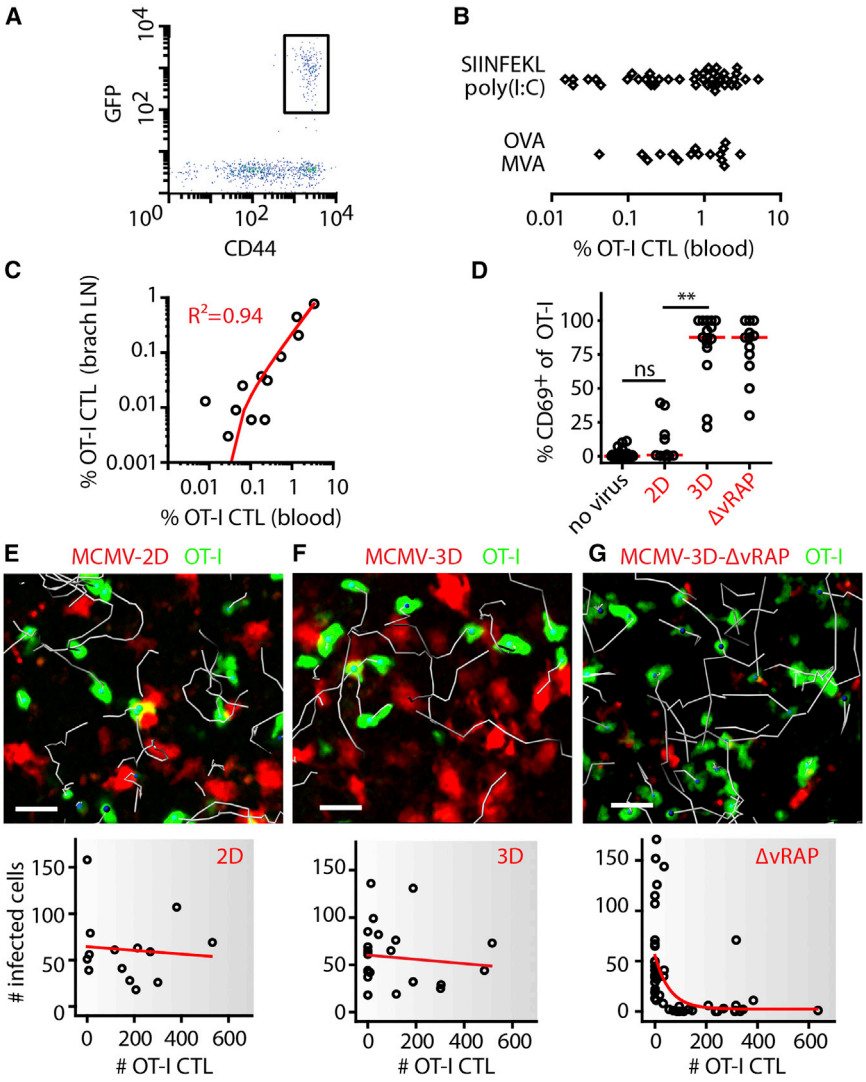

Figure 2. Cytotoxic T lymphocytes Fail to Kill Infected Cells Protected by Viral MHC-I Immune Evasion

Protocol for generation of CTLs: 10^5 naive FP-expressing OT-I cells were transferred into C57BL/6 mice and activated at day 1 by different protocols. After expansion, different MCMV strains were injected into the footpad, and two-photon microscopy was used for studying CTL behavior and the number of infected cells in the draining popliteal lymph node.

(A) On day 5 after priming, all GFP$^+$ FP-OT-I CTLs expressed CD44 after expansion. Flow cytometry was gated on all blood CD8$^+$ T cells.

(B) The percentage of FP-OT-I CTLs (of total leukocytes) in blood after priming by different protocols (data were pooled from at least six independent experiments).

(C) The percentage of OT-I CTLs in blood is plotted against the percentage of OT-I CTLs found in brachial lymph nodes. Dots represent lymph nodes, and the red line represents linear regression. Data were pooled from three independent experiments.

(D) One day after infection, OT-I CTLs in the popliteal lymph node were stained for surface CD69 expression. MCMV-2D (2D) was used as a SIINFEKL-negative control, and Kruskal-Wallis and Dunn's tests were used for comparing multiple groups. Dots represent lymph nodes, and red lines represent medians. Data were pooled from at least three experiments. **$p < 0.01$; ns, not significant.

(E–G) One day after infection with the viruses indicated, OT-I CTLs were observed in regions harboring infected cells (upper panel), and numbers of infected cells were counted (lower panel). In the upper panels, 10 min tracks are shown in gray, and scale bars represent 20 μm. In the lower panels, dots represent lymph nodes, and lines represent linear regression (E and F) or one-phase exponential decay (G). Data were pooled from at least six experiments.

CTL priming was performed with SIINFEKL and poly(I:C) in (C)–(G).

findings indicate that induction and execution of pro-apoptotic signaling cascades in virus-infected cells does not ensue instantaneously after a single CTL contact but that the accumulation of multiple CTL contacts determines the fate of virus-infected cells.

Different Virus-Infection Models Reveal Low Average CTL PCKRs

To study CTL-mediated killing in another infection model, we generated two reporter strains of the poxvirus MVA (Kremer et al., 2012). Injection of MVA-mCherry into the footpad led to infection of CD169$^+$ subcapsular sinus macrophages in the draining lymph node (data not shown). OT-I CTLs killed MVA-OVA-mCherry- but not MVA-mCherry-infected cells (Figure 5A; Movie S3). As observed during MCMV-3D-ΔvRAP infection, CTLs within the MVA-OVA-mCherry-infected lymph nodes showed reduced track speed (Figure 5B), antigen-triggered dynamic contacts (Figure 5C), and disruption of targets that depended on CTL density at the site of infection (Figure 5D).

To quantify CTL-mediated killing of the different virus-infected cells, we analyzed the expression kinetics of the mCherry reporter to test whether detection of all infected cells can be expected during the two-photon imaging time windows. In vitro infection revealed stronger and faster mCherry expression by MVA at 4–8 hr after infection (Figures S2A–S2D), whereas after 12 hr, both MVA and MCMV were robustly detectable both in vitro and in the infected lymph node (Figures S3A–S3D; Movie S4). Furthermore, virus-specific CTLs could already recognize their specific virus-encoded peptide at 8 hr after infection (Figures S3D and S3E). Thus, direct observation of single CTLs and single virus-infected cells was feasible from 12–24 hr after infection.

Next, we used two-photon-microscopy-derived datasets from the different virus-infection models to calculate PCKRs of OT-I CTLs, i.e., the theoretical average number of infected cells killed per CTL per day (Elemans et al., 2012). PCKR values reported in the literature are highly variable and were calculated on the basis of indirect assays or on assays relying on adoptively transferred

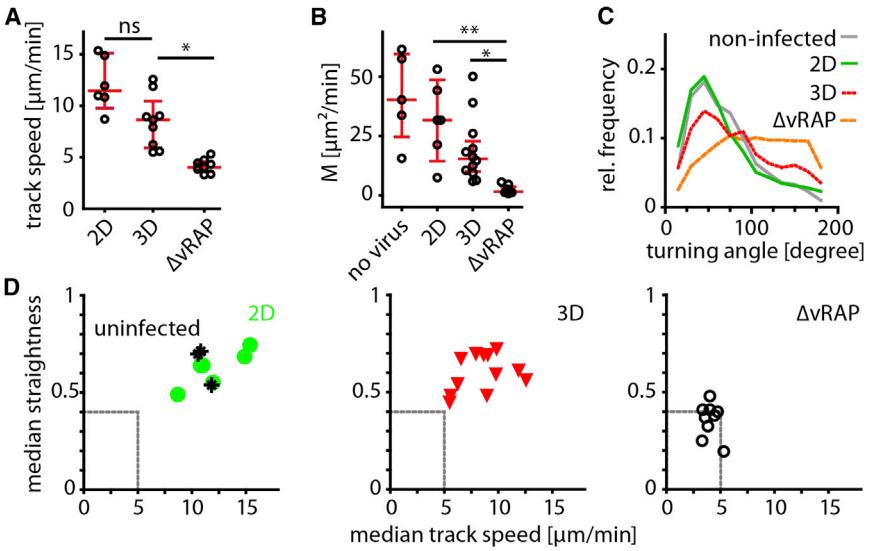

Figure 3. Cognate Antigen Presentation and Viral Immune Evasion Determine the Migration Behavior of CTLs while Attacking Virus-Infected Cells

(A–C) One day after infection, two-photon microscopy was used to quantify OT-I CTL track speed (A), motility coefficient, (B) and turning angles (C) in movies with intact MCMV-infected cells. Dots represent median values from all tracks per movie, and red bars represent IQRs. Kruskal-Wallis and Dunn's tests were used for comparing multiple groups. Data were pooled from two to six independent experiments per condition. *$p < 0.05$; **$p < 0.01$; ns, not significant.

(D) OT-I CTL population median track straightness (y axis) was compared to median track speed (x axis) per imaging region (dots represent median track straightness and median track speed for the different viruses per mouse).

CTL priming was performed with SIINFEKL and poly(I:C); see also Figure S1.

artificial targets (Elemans et al., 2012; Regoes et al., 2007). On the basis of our direct observation of endogenous virus-infected cells killed, here we calculated PCKRs of 4.8 (median, MCMV-3D-ΔvRAP) and 4.2 (median, MVA-OVA-mCherry; Figure 5E). Notably, viral MHC-I immune evasion of MCMV-3D reduced the PCKR to 0.0 (median), thus resembling infection with MCMV-2D (Figure 5E). Together, direct visualization and quantification revealed that the OT-I CTL population showed a limited killing efficiency in different infection models and that viral MHC-I immune evasion dramatically reduced CTL killing efficiency in vivo.

Intralymphatic CTL Transfer and Mathematical Modeling Confirm Low Killing Rates

To determine whether CTLs generated from the endogenous pool of $CD8^+$ T cells show killing efficiencies similar to those of TCR-transgenic $CD8^+$ T cells, we generated CTLs in wild-type or perforin-deficient B6 mice ($Prf^{-/-}$) by intraperitoneal infection with MCMV-3D. After 6–8 days, MCMV-specific CTLs were isolated by tetramer staining (Altman et al., 1996). Employing our previously developed technique of intralymphatic injection (Braun et al., 2011), we delivered tetramer-enriched (~60% purity) or tetrameter-sorted (90% purity) CTLs or negatively enriched CTLs (depletion of $CD62L^{hi}$ and non-$CD8^+$ T cells) into the afferent lymphatic vessel draining toward the popliteal lymph node of MCMV-3D-ΔvRAP-infected mice. One day after intralymphatic transfer, we found that the reduction of virus-infected cell numbers, i.e., killing of targets, was dependent on the local number of B6 CTLs (Figures 6A and 6B). Similar to B6 CTLs, tetramer-sorted $Prf^{-/-}$ CTLs showed the typical migration behavior during target cell attack but were unable to disrupt virus-infected cells (Figure 6C; Movie S4).

To quantify CTL killing efficiencies after intralymphatic injection, we used a mathematical model to describe the killing of virus-infected cells at different CTL densities 0–24 hr after infection (Supplemental Experimental Procedures; Figure 6D). This model makes no assumptions on CTL killing mechanisms and has been developed in accordance with published modeling approaches (reviewed in Elemans et al., 2012, and Regoes et al., 2007). Furthermore, this model calculates average PCKR values for the entire CTL population, and the results obtained can be directly compared to the counting approach described in Figure 5. Applying this simple mathematical model, we calculated PCKRs from 2.0 to 10.4 for tetramer-enriched, tetramer-sorted, or negatively selected polyclonal CTLs (Figure 6E). In contrast, $Prf^{-/-}$ CTLs showed a PCKR close to 0 (Figure 6E). Thus, PCKRs obtained by intralymphatic transfer of in-vivo-primed CTLs and mathematical modeling were in agreement with the PCKRs obtained by real-time two-photon imaging, together arguing for a limited average PCKR for CTLs attacking virus-infected cells.

Low In Vivo CTL-Mediated Killing Rates in the Dermis

Because CTL killing efficiency might be different in a non-lymphoid organ, we next studied CTL killing in the dermis of T-cell-deficient mice ($Cd3e^{-/-}$; $Rag2^{-/-}$). These animals were reconstituted with FP-OT-I or FP-$CD8^+$ T cells. Intraperitoneal virus infection was then used to prime and expand T cells (Figure S4A). In vivo two-photon microscopy showed that 1 day after secondary s.c. ear infection with MCMV-3D-ΔvRAP, but not after infection with MCMV-3D, OT-I CTLs migrating around infected dermal fibroblasts were found to exhibit the typical dynamic scanning behavior characterized by low track speed and low motility coefficients (Figures S4B–S4D). Likewise, mice reconstituted with polyclonal $CD8^+$ T cells and primed intraperitoneally with MCMV-3D displayed CTLs characteristically scanning infected cells in the dermis, as well as local eradication of MCMV-3D-ΔvRAP-infected targets (Figures S4E–S4G; Movie S5). In the skin, we observed median PCKRs of 16.0 and 12.5 for OT-I and polyclonal CTLs, respectively (Figure S4H). Thus, two-photon in vivo imaging of the infected skin supports the conclusion that CTLs show limited killing efficiency when attacking virus-infected stromal cells.

Calcium Signaling in Virus-Infected Cells Reveals Heterogeneity of Single CTL-Contact Events

It is currently unclear whether all CTLs specific to the same epitope show the same killing rate or whether some CTLs kill

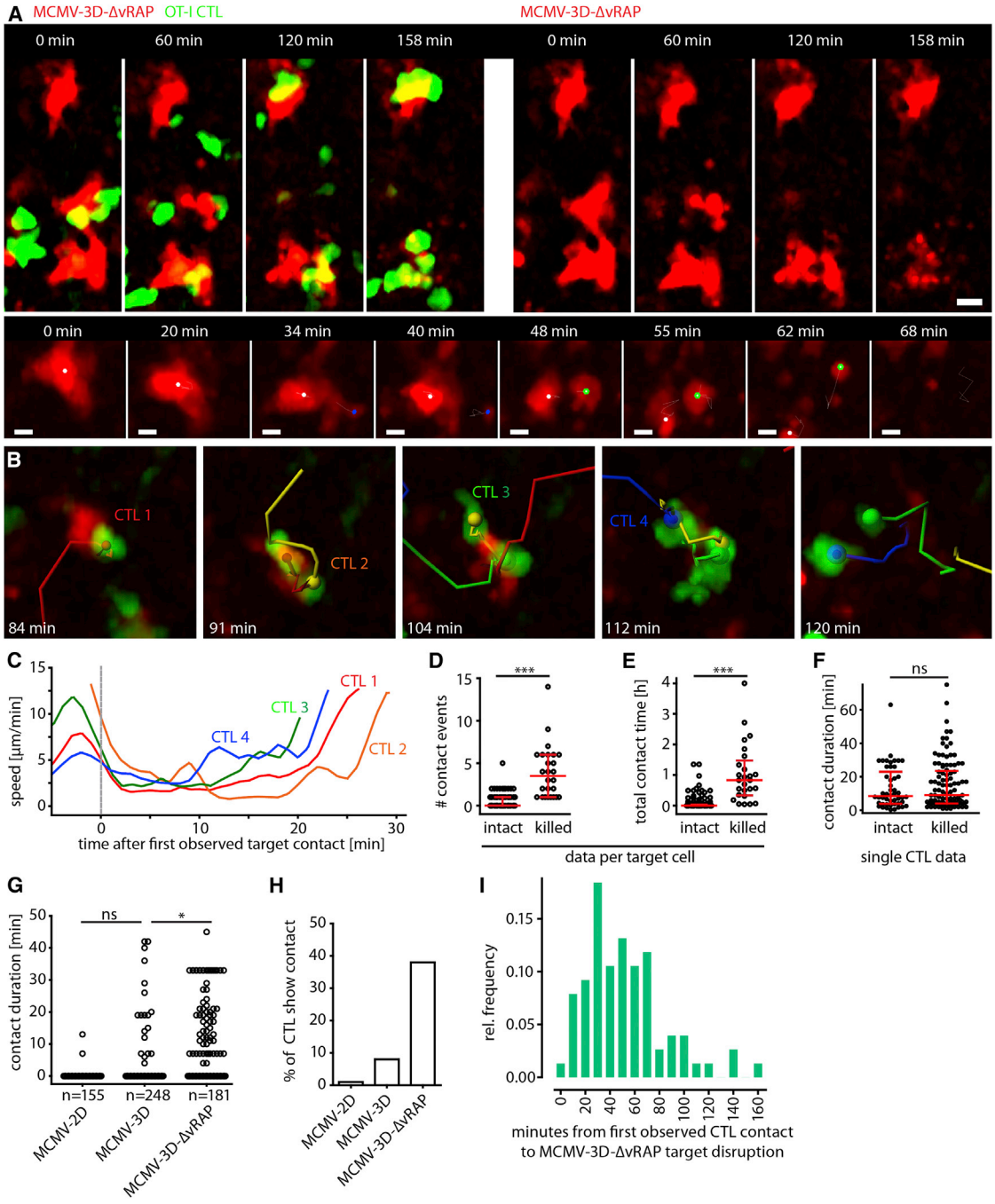

Figure 4. Two-Photon Microscopy Allows for Real-Time Visualization of CTL-Mediated Killing of Virus-Infected Cells

(A) Upper panel: two-photon microscopy revealed disruption of mCherry$^+$ infected cells (red) and contact events by OT-I CTLs (green) 14 hr after MCMV-3D-ΔvRAP infection of mice harboring FP-CTLs (elapsed time displayed). Scale bar represents 20 μm. Lower panel: example of mCherry$^+$ cell-body morphology during disruption (CTLs not shown). Dots represent center spots of original cell and large fragments. Scale bar represents 5 μm.

(B) Example of four CTLs (red, orange, green, and blue tracks) that interacted with one virus-infected target (red).

(C) Instantaneous speed of the four CTLs shown in (B).

(D) Number of OT-I CTL contacts (>1 min) with MCMV-3D-ΔvRAP-infected target cells that survived (intact) or were killed during the observation period of 1–3 hr. Dots represent target cells. ***$p < 0.001$.

(E) Cumulative CTL-contact duration per target cell. Dots represent target cells. ***$p < 0.001$.

(F) Duration of individual CTL-contact events. Dots represent CTL contacts. ns, not significant.

(D–F) Red bars represent the median with IQR, and data were pooled from nine movies from four independent experiments. A Mann-Whitney test was used for comparing intact and killed target cells.

(legend continued on next page)

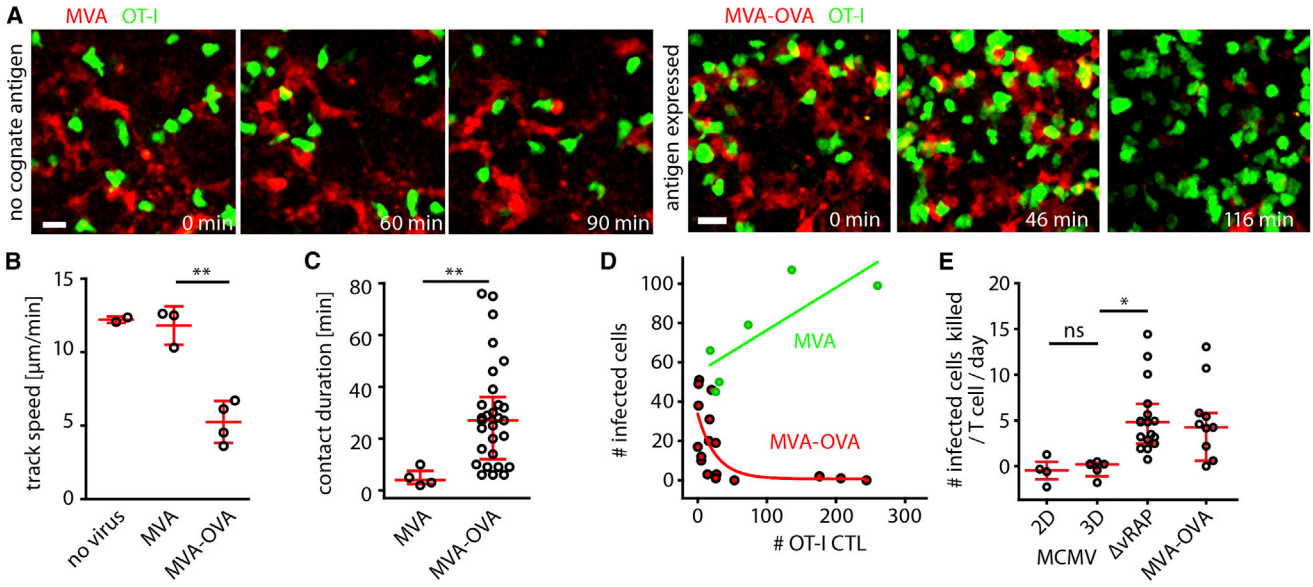

Figure 5. CTLs Show Low Average PCKRs in Both Poxvirus and Cytomegalovirus Infection Models

Experimental setup for two-photon imaging of MVA-infected lymph nodes: transfer of FP-OT-I (day 0), expansion with SIINFEKL plus poly(I:C) (day 1), infection with MVA or MVA-OVA (day 6), and two-photon imaging (day 7).

(A) One day after footpad infection with MVA or MVA-OVA (10^7 PFU), two-photon microscopy was used for observing OT-I CTLs (green) at the site of MVA-infected mCherry$^+$ cells (red).

(B) Median track speed of the OT-I CTL population in non-infected or MVA- or MVA-OVA-infected lymph nodes. Dots represent the mean of >50 CTLs analyzed per lymph node, and red bars represent the mean ± SD. A t test with Welch's correction was used for comparing MVA and MVA-OVA. **$p < 0.01$.

(C) OT-I CTL contacts with MVA- or MVA-OVA-infected cells were analyzed. Dots represent contact duration per CTL, and red bars represent IQRs. A Mann-Whitney test was used for comparing MVA and MVA-OVA. **$p < 0.01$.

(D) One day after infection, the number of OT-I CTLs and MVA-infected cells per imaging region was correlated (green dots, MVA infection; green line, linear regression; red dots, MVA-OVA infection; red line, one-phase exponential decay). Dots represent individual mice (B), cells (C), and lymph nodes (D). Data were pooled from three independent experiments in (B)–(D). Scale bars represent 20 µm.

(E) OT-I CTLs PCKRs were calculated from automated-cell-tracking data for different MCMV and MVA strains. Dots represent movies, and red bars represent IQRs. A Kruskal-Wallis test was used for comparing multiple groups (outliers are not shown but were included in the test). *$p < 0.05$; ns, not significant.

more efficiently than others. Thus, we first tested whether all CTLs that are in contact with infected cells show signs of activation. Using OT-I CTLs expressing retrovirally transduced nuclear factor of activated T cells (NFAT)-GFP (Aramburu et al., 1998) and H2B-mOrange reporter constructs, and assuming that cognate recognition results in nuclear NFAT translocation within 1–3 min (Marangoni et al., 2013), we addressed whether CTLs in contact with infected cells can readily recognize the target. After MCMV-2D or -3D infection, the NFAT-GFP fluorescent signals remained in the CTL cytoplasm, which is in agreement with the absence of killing of these virus variants. In contrast, after MCMV-3D-ΔvRAP infection, 80% of CTLs in contact with infected cells—but also some CTLs not in contact with targets—showed nuclear NFAT-GFP (Figures S5A–S5D; Movie S6; data not shown). Thus, CTLs were usually activated during target-cell contact. However, because CTLs frequently retained the NFAT signal in the nucleus after target disengagement (Marangoni et al., 2013), NFAT signaling did not allow us to distinguish between CTLs with different killing rates.

Perforin pores in the plasma membrane have been suggested to trigger a transient calcium (Ca^{2+}) flux in the target cell (Keefe et al., 2005). To gain further insights into the functional heterogeneity of CTLs, we therefore qualitatively and quantitatively analyzed CTL-induced Ca^{2+} influx in infected targets. To study Ca^{2+} fluxes in virus-infected cells, we replaced the luciferase-encoding sequence of MCMV-3D and MCMV-3D-ΔvRAP with a sequence encoding the ultra-sensitive Ca^{2+} sensor GCaMP6s (Chen et al., 2013), resulting in the reporter viruses MCMV-3D-Ca and MCMV-3D-ΔvRAP-Ca, respectively (Figures S6A–S6C). After footpad infection of non-immunized B6 mice with MCMV-3D-Ca or MCMV-3D-ΔvRAP-Ca, most infected cells showed spontaneous short Ca^{2+} fluxes that lasted on average 6 s (median; Figures 7A–7D; Movie S7). After infection with MCMV-3D-ΔvRAP-Ca, OT-I CTLs dynamically interacted with

(G) Duration of OT-I CTL contact with MCMV-2D-, MCMV-3D-, and MCMV-3D-ΔvRAP-infected cells. Here, data from CTLs not in contact with infected cells are shown (independent analysis of dataset used in D–F). *$p < 0.05$; ns, not significant.

(H) Percentage of CTLs that showed target-cell contact (data from G).

(I) Time from first observed CTL contact to death of MCMV-3D-ΔvRAP-infected cells. Target-cell death was defined as complete target disintegration, as shown in (A) and (B) (relative frequencies and binned data from 76 killed infected cells from four independent experiments are shown).

CTL priming was performed with SIINFEKL and poly(I:C) in (A)–(H). In (I), data with MVA-OVA priming was also added; see also Figures S2, S3, and S4.

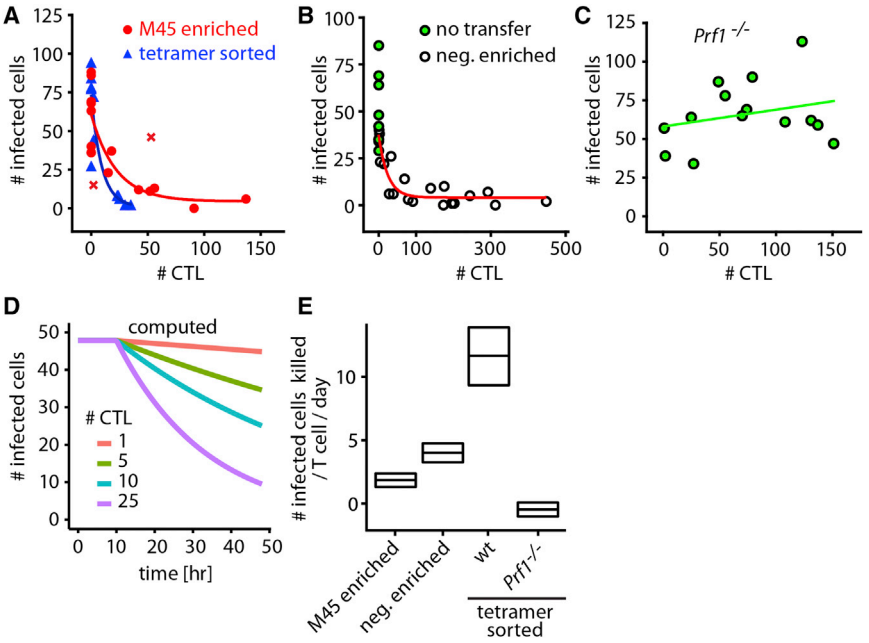

Figure 6. Intralymphatic CTL Transfer and Mathematical Modeling Show Low Killing Rates

Protocol for intralymphatic transfer: MCMV-3D-ΔvRAP footpad infection (0 hr), intralymphatic injection of different types of CTLs (~4 hr), and two-photon imaging of single time points (~24 hr).

(A) One day after infection and intralymphatic delivery of M45-tetramer-enriched CTLs (red) or M45-, M38-, and M139-tetramer-sorted CTLs (blue), the number of MCMV-3D-ΔvRAP-infected cells and CTLs per imaging region was counted from images of single time points.

(B) Same as (A) either without cell transfer or after injection of negatively enriched CTLs (magnetic depletion of $CD62L^{hi}$ and non-$CD8^+$ T cells).

(C) Same as (A) after injection of perforin-deficient tetramer-sorted CTLs.

(A–C) Data pooled from seven independent experiments (dots represent lymph nodes, and lines represent exponential decay). CTL priming was performed with intraperitoneal infection of CTL-donor mice with MCMV-3D.

(D) Mathematical modeling calculating the kinetics of infected cell numbers in a standard imaging region at the infected site of the lymph node cortical sinus, depending on the number of CTLs present (plot of infected cell numbers over time).

(E) The number of infected cells killed per T cell per day (PCKR) for the different CTL populations was calculated by the mathematical model from the raw data (median and 95% confidence interval) shown in (A)–(C). See Supplemental Experimental Procedures for details on the mathematical model.

and triggered long-lasting Ca^{2+} fluxes in infected targets (Figures 7E–7G; Movie S7). CTL-induced Ca^{2+} fluxes lasted for 80 s (median; interquartile range [IQR] = 40–240 s; Figures 7E–7G) and started 480 s (median) after CTL encounter (IQR = 60–820 s; Figure 7H). Although CTLs intensively contacted infected cells, 40% failed to induce a long-lasting Ca^{2+} flux (Figure 7I), and only 10% of CTLs induced three or four death-associated Ca^{2+} fluxes (Figure 7J). Perforin-deficient CTLs failed to elicit long-lasting Ca^{2+} fluxes and cell death (Figure 7K; Figure S6D). Together, these findings reveal that individual CTLs and CTL contacts targeting virus-infected cells show strong functional heterogeneity.

Cytotoxic T Lymphocytes Cooperate during Killing of Virus-Infected Cells

Because single CTL contacts frequently failed to trigger long-lasting Ca^{2+} influx or death of target cells, we next addressed whether CTLs cooperate while killing virus-infected cells. In all of the above-described imaging models, virus-infected cells were disrupted more frequently when they were contacted by several rather than single CTLs. To test for CTL cooperativity, we choose a null hypothesis that assumed that every CTL contact is an independent event and that previous contacts do not influence the target cell's death probability. This Bernoulli-series null hypothesis states that the probability p(n) that a target cell will die after n interactions is given by the term $p(n) = 1 - (1 - p(1))^n$. Data from 660 individual MCMV-3D-ΔvRAP-infected target cells were grouped according to the total number of CTL contacts observed per target cell. Targets without any observed CTL interactions died with a probability of p(0) = 0.01, whereas targets with a single or two CTL contacts died with a probability of p(1) = 0.15 or p(2) = 0.28, respectively. In the case of three or five CTL contacts, the probability that an infected cell would die was significantly higher than predicted from the null hypothesis of independent interaction outcomes (Figures 7L and 7M). Thus, CTLs were able to cooperate to kill virus-infected cells by increasing the probability of target cell death after multiple CTL encounters.

DISCUSSION

In the present study, we visualized how CTLs killed virus-infected cells in vivo. We used MCMV and MVA reporter constructs that, after s.c. injection, infected draining lymph node stromal cells and subcapsular sinus macrophages, respectively. Because all reporter viruses encoded mCherry, we could clearly identify single infected cells and use time-lapse ex vivo and in vivo two-photon microscopy to determine their fates after they were contacted by effector $CD8^+$ T cells.

Two-photon imaging revealed that in most situations, migrating CTLs do not come to a complete arrest to establish a static synapse with their target. Stable and static synapses have been described in lymph nodes (1) in vivo between antigen-presenting cells and T cells during defined stages of T cell priming and (2) in vitro on coated surfaces between CTLs and targets (Mempel et al., 2004; Ritter et al., 2015). As described for static synapses, the formation of dynamic kinapses observed in the present study also relied on the cognate interaction between TCR and MHC-I-presented antigen, because kinapses do not form between OT-I CTLs and cells infected with MCMV-2D (no cognate antigen) or MCMV-3D (low surface MHC-I expression). Among other factors, the formation of static immunological synapses has been shown to depend on integrin activation, which allows firm adhesion and complete arrest of migrating cells (Liu et al., 2009). Interestingly, treatment of

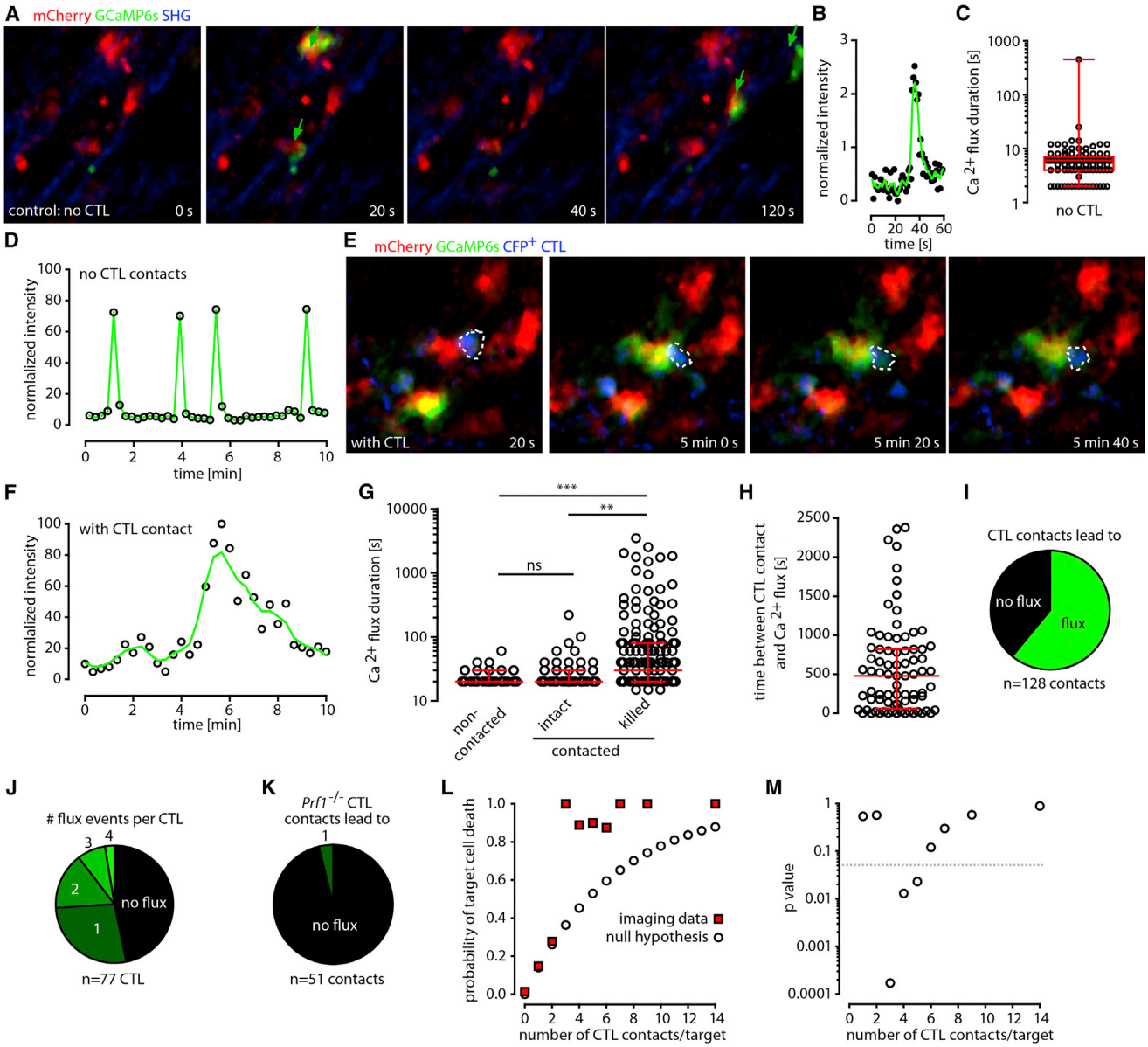

Figure 7. CTLs Trigger Ca^{2+} Fluxes in Virus-Infected Cells and Cooperate during Killing

(A) One day after infection with MCMV-expressing Ca^{2+} sensor GCaMP6s (MCMV-3D-ΔvRAP-Ca), two-photon microscopy was used to record GCaMP6s intensity (green) in virus-infected cells (red).

(B) Kinetics of GCaMP6s intensity in an infected cell imaged at 0.2 Hz.

(C) Ca^{2+} flux (defined as $GCaMP6s^{bright}$ event) duration in virus-infected cells in the absence of specific CTLs (dots represent cells, and red bars represent IQRs; n = 98 infected cells from three mice).

(D) Kinetics of Ca^{2+} fluxes in one infected cell imaged for 10 min at 0.07 Hz.

(E) In lymph nodes with MVA-OVA-primed CTLs present, a CFP^+ OT-I CTL (blue; dotted line) contacted a MCMV-3D-ΔvRAP-Ca-infected cell (long flux defined as $GCaMP6s^{bright}$ event lasting >30 s).

(F) Kinetics of a long-lasting Ca^{2+} flux of an infected cell imaged for 10 min at 0.05 Hz. The green line represents the locally weighted scatterplot smoothing curve.

(G) Duration of Ca^{2+} fluxes of infected cells that were not contacted, were contacted but stayed intact, or were contacted and killed. Dots represent cells, and red bars represent IQRs. A Kruskal-Wallis test was used for comparing multiple groups. Data were pooled from four experiments from six different mice for a total of 307 flux events analyzed. $^{**}p < 0.01$; $^{***}p < 0.001$; ns, not significant.

(H) Time interval between CTL contact and subsequent long-lasting Ca^{2+} flux (n = 79 events from four experiments analyzed; red bars represent IQRs).

(I) Percentages of CTL contacts that were followed by a long-lasting Ca^{2+} flux (n = 128 CTLs). Data were pooled from four experiments.

(J) Percentages of different numbers of long-lasting Ca^{2+} fluxes that followed a CTL contact event (n = 77 CTLs). Data were pooled from four experiments.

(K) Percentage of long-lasting Ca^{2+} fluxes that followed contacts of $Prf^{-/-}$ CTLs (n = 51 contacts pooled from three experiments).

(L) Probability of target-cell death for infected cells contacted by 0–14 CTLs. Hypothetical values for the no-cooperativity null hypothesis (open dots) and observed data (red squares) are provided. In total, 660 infected cells were analyzed, and data were pooled from >12 independent experiments.

(M) p values for comparing data derived from the null hypothesis and observed data (0.05 significance level indicated by dotted line); see also Figures S5, S6, and S7.

mice with neutralizing antibodies against β1- and β2-integrin or injection of CTLs lacking the TCR adaptor protein ADAP, involved in TCR signaling leading to integrin activation, did not show differences in the slow but dynamic CTL migration behavior during the attack on infected cells or during the faster migration when CTLs were not contacting infected target cells (Figure S7). Therefore, integrin-independent formation of dynamic kinapses might represent a mechanism that not only allows CTLs to deliver the content of their cytotoxic granules but also keeps them in a motile state to successfully search for further targets.

By recruiting effector cells to the site of infection, chemokine receptors such as CXCR3 and CCR5 have been shown to contribute to CTL function (Hickman et al., 2015; Kastenmüller et al., 2013). In the present study, we observed no significant difference between wild-type and CXCR3- or CCR5-deficient CTLs regarding killing efficiencies in the intralymphatic transfer model (data not shown). These findings indicate that the mode of CTL delivery, the strain of virus investigated, and the cell type infected might affect the differential requirement for chemokine receptors for CTL recruitment. In our study, CTL attack on virus-infected cells resembled the behavior of NK cells attacking tumor cells (Deguine and Bousso, 2013).

In addition to assessing cell disruption on the basis of changes in cell morphology, we used the genetic Ca^{2+} sensor GCaMP6s expressed in the target cell to better understand CTL-mediated killing. Earlier in vitro studies have suggested that perforin pores in the plasma membrane of target cells cause a transient Ca^{2+} influx that is sensed by the cells as a sign to repair plasma-membrane damage (Keefe et al., 2005; Thiery et al., 2011). In virus-infected cells, expression of GCaMP6s proved a sensitive and reliable indicator of Ca^{2+} fluctuations. In the absence of natural killer cells and CTLs, virus-infected cells showed spontaneous short Ca^{2+} fluxes (data not shown), whereas CTL-induced fluxes could last for several minutes and reliably indicated subsequent cell death. Our study revealed that, on average, 8 min elapsed between CTL contact and Ca^{2+} influx, whereas subsequent cell disruption occurred in most situations between 20 and 120 min after the first CTL contact. In one study, in vivo imaging revealed killing of lymphoid cells within 10–20 min of CTL contact (Mempel et al., 2006), whereas other studies failed to observe rapid killing of virus-infected keratinocytes, malaria-infected hepatocytes, or tumor cells (Breart et al., 2008; Cockburn et al., 2013; Hickman et al., 2013). Notably, when CTLs attack peptide-pulsed B cells, additional B cell surface molecules (such as SLAMF7) could strengthen the CTL attachment and affect CTL behavior during killing. Together, the specific tropism of the pathogen and the targeted cell type essentially contribute to the outcome of CTL-mediated immune reactions.

The control of virus infection is critically determined by the quality of the CTLs generated (Plotkin, 2013; Varadarajan et al., 2011). CTLs can be heterogeneous with regard to the expression of effector molecules as well as the expression of co-stimulatory or inhibitory surface molecules (Jenkins et al., 2008; Newell et al., 2012). The data shown here also reveal that CTLs are heterogeneous with regard to nuclear translocation of the transcription factor NFAT after cognate antigen recognition. Furthermore, CTLs are highly diverse with regard to their ability to induce death-associated Ca^{2+} influx in target cells; for example, in movies with an average duration of 66 min, 40% of the CTLs were unable to trigger Ca^{2+} influx, whereas 10% induced three or four Ca^{2+} fluxes. This functional CTL heterogeneity helps to explain the observed overall low average killing rates.

The local presence of antigen-specific regulatory T cells can affect CTL killing efficiency (Mempel et al., 2006). The presence of immune-suppressive cells might also explain why intralymphatically delivered tetramer-enriched cells kill slightly less efficiently than very pure tetramer-sorted CTLs.

Two-photon microscopy allowed us to analyze the fate of single infected cells with regard to their CTL-contact history. This approach revealed that CTLs exhibited cooperativity in killing targets when more than two CTLs contacted the infected cell. The underlying mechanisms for this observation are unclear but could be explained by the differential expression levels of granzymes and perforin (and potentially other molecules) in individual CTLs (Jenkins et al., 2008). Two CTL contacts did not result in detectable signs of cooperativity, maybe because the effect of two CTL contacts is too small to be revealed in the assay setup used. In general, if we assume the existence of CTLs with a high or low killing capacity, it is plausible that multiple contacts increase the probability that a fully armed CTL actually disintegrates the infected cell. Alternatively or additionally, it seems possible that the accumulation of sub-lethal pro-death signals delivered by different single CTLs might lead to faster apoptosis of the target. Together, our data show that CTL cooperativity helps to combat viral infections.

The average killing efficacy of individual CTLs crucially affects the outcome of infectious diseases relying on CTL-mediated killing as a main control mechanism. There is currently no consensus on even the order of magnitude of in vivo CTL killing rates in either experimental models or human diseases (Elemans et al., 2014; Elemans et al., 2012; Hickman et al., 2013). Estimated killing rates of mouse and human CTLs vary considerably, and it is unknown how much the different viruses studied, the vaccination protocols applied to CTL generation, or the killing assays used affect the killing estimates (Garcia et al., 2015). Further complicating matters, the definition of killing rates often relies on different rate constants, not taking into account the number of CTLs that might be responsible for the killing (Ganusov and De Boer, 2008).

We therefore chose to calculate the average number of virus-infected cells killed per CTL per 24 hr as a simple measure of the CTL-mediated killing to allow direct comparison between different models. We determined killing rates either by directly observing disintegration of infected cells over time by a defined CTL population size or by determining the ratio of CTLs and infected cells at given time points after infection. The PCKRs calculated by these approaches give an average value that describes the killing efficiency of the whole CTL population (and not of individual CTLs) without assumptions about CTL cooperation or the percentage of non-active CTLs. Strikingly, our data show a consistent range of 2–16 infected cells killed per CTL per day, irrespective of the investigated epitopes recognized by the CTL, the method of calculation (counting or mathematical modeling), the type of cell infected (macrophages or stromal cells), or the virus used (MVA or MCMV-3D-ΔvRAP).

Because two-photon imaging cannot detect killing events that might occur before imaging is started, the PCKR values from *direct* imaging-based counting might slightly underestimate killing efficiencies. However, killing of "non-visible" cells does not affect our mathematical model, because the time point of killing is not important in this experimental setup. Both direct counting and mathematical modeling might have limitations, but all PCKR estimates obtained here (from different viruses infecting different cells, different organs, and by different methods) are consistent in that they range from 2 to 16 target cells killed per CTL per day.

It remains unknown for how long a single CTL can maintain a certain killing rate, and it will be interesting to measure whether single CTL killing rates increase or decrease after sequential target-cell encounter.

All together, our data indicate that the average in vivo CTL killing capacity is rather limited and not in agreement with the assumption that all CTLs act as "rapid" and "serial" killers that destroy hundreds or thousands of targets per day (Elemans et al., 2012). Therefore, protective CTL immunity might require substantially higher CTL densities than previously thought. This can possibly explain the failure of some CTL-based vaccines (Plotkin, 2013; Yewdell, 2010) or the development of chronic viral infections (West et al., 2011), in which functional CTLs are initially present but fail to eradicate all virus-infected cells.

EXPERIMENTAL PROCEDURES

MCMV Strains

All MCMV strains were derived from the pSM3fr Smith strain (cloned as a bacterial artificial chromosome) and were produced and titrated in vitro according to standard techniques (Marquardt et al., 2011). GCaMP6s-expressing MCMV strains were designed with plasmid pGP-CMV-GCaMP6s (Chen et al., 2013) obtained from Addgene (plasmid 40753). See Supplemental Experimental Procedures for details.

MVA Strains

MVA-mCherry and MVA-OVA-mCherry were generated by homologous recombination using the plasmid vectors pIIIdHR-P7.5 and pLW-73 according to standard procedures. See Supplemental Experimental Procedures for details.

Mice

C57BL/6 (B6) mice were bred at the central animal facility at Hannover Medical School under specific-pathogen-free conditions or purchased from Charles River or the Jackson Laboratory (JAX). Female or male mice were used at the age of 6–18 weeks. The following mutant B6 mouse strains were used: C57BL/6-Tg(CAG-EGFP) (JAX 003291) mice expressing GFP under an artificial CMV-actin-globin promoter (here named GFP), C57BL/6-Tg(CAG-eCFP) mice expressing CFP under the beta-actin promoter (JAX 004218), TCR-transgenic OT-I CD45.1$^+$ mice (derived from C57BL/6-Tg(TcraTcrb)1100Mjb/J; JAX 003831), F1-cross between GFP and OT-I CD45.1$^+$ (named FP-OT-I), *Adap*$^{-/-}$ mice (C57BL/6J Fyb × B6.PL-Thy1a/CyJ × B6-Tg(TcraTcrb)1100Mjb), *Cd3e*$^{-/-}$ mice (C57BL/6-CD3etm1Mal/Orl), *Prf1*$^{-/-}$ mice (JAX 002407), and *Rag2*$^{-/-}$ mice (JAX 008449). All experiments were conducted in accordance with the local animal welfare regulations reviewed by the institutional review board and the Lower Saxony State Office for consumer protection and food safety (LAVES).

Generation of OT-I CTLs In Vivo

CD8$^+$ T cells from OT-I mice, containing 10^5 CD8$^+$ TCR Vα5$^+$ OT-I cells, were transferred into recipient mice. OT-I CTL priming was performed by different regimes. See Supplemental Experimental Procedures for details.

Intralymphatic Injection of CTLs

Two to six hours after MCMV-3D-ΔvRAP infection, 2.5×10^4 to 1×10^5 CTLs diluted in 5 μl PBS were injected in 90 s into the afferent lymph vessel draining toward the popliteal lymph node, as described before (Braun et al., 2011).

Two-Photon Microscopy

Ex vivo two-photon imaging was performed with custom-build chambers for imaging explanted lymph nodes, as described in Halle et al. (2009). In Figure S4, the skin at the site of infection in the ear of anesthetized mice was imaged directly in vivo. See Supplemental Experimental Procedures for details.

Calculation of Average CTL Killing Rates

We calculated the number of infected cells killed per T cell per day on the basis of the observed time course of the number of killed virus-infected cells and the average number of CTLs in two-photon microscopy movies. Data from independent experiments were pooled, and average killing rates were reported. Alternatively, we used the single-time-point imaging data from the intralymphatic injection together with the mathematical model to calculate average CTL killing rates and 95% confidence intervals. See Supplemental Experimental Procedures for details.

Statistical Analysis

Statistical analysis was performed with GraphPad Prism 4. When comparing two groups, we calculated p values with the nonparametric Mann-Whitney test. To compare multiple groups, we used the Kruskal-Wallis test with Dunn's test. All data were pooled from multiple independent experiments. See Supplemental Experimental Procedures for details.

SUPPLEMENTAL INFORMATION

Supplemental Information includes Supplemental Experimental Procedures, seven figures, and seven movies and can be found with this article online at http://dx.doi.org/10.1016/j.immuni.2016.01.010.

AUTHOR CONTRIBUTIONS

S.H., F.R.S., X.Z., K.H., J.B., K. Wagner, Y.B., R.M., A. Braun., K. Werth, and R.A. performed the experiments; K.A.K., A. Busche., A.M., M.G., V.H., M.K., G.S., and M.M. designed and produced the different viral constructs and virus strains; A.U., H.K., and M.M.-H. designed and applied the mathematical models; and S.H. and R.F. designed the experiments and wrote the manuscript.

ACKNOWLEDGMENTS

This study was supported by DFG grant SFB 900-B1 to R.F. and M.M., ERC advanced grant 322645-LYMPHATICS-HOMING to R.F, the Niedersachsen Research Network on Neuroinfectiology, N-RENNT to R.F., a Lichtenberg stipend to F.R.S., and a Boehringer-Ingelheim stipend to A. Braun. A.U. and M.M.-H. were supported by the German Federal Ministry of Education and Research (BMBF) within the Measures for the Establishment of Systems Medicine (eMed) project Systems Immunology and Image Mining in Translational Biomarker (SYSIMIT). H.K. and M.M.-H. were supported by the Human Frontier Science Program. We thank Mathias Herberg for excellent animal handling and Immo Prinz, Andreas Krueger, and Olga Kristina Halle for reading and commenting on the manuscript. We would like to acknowledge the expert assistance of the Cell Sorting Core Facility of Hannover Medical School.

Received: July 6, 2015
Revised: October 8, 2015
Accepted: November 18, 2015
Published: February 9, 2016

REFERENCES

Altman, J.D., Moss, P.A., Goulder, P.J., Barouch, D.H., McHeyzer-Williams, M.G., Bell, J.I., McMichael, A.J., and Davis, M.M. (1996). Phenotypic analysis of antigen-specific T lymphocytes. Science *274*, 94–96.

Aramburu, J., Garcia-Cózar, F., Raghavan, A., Okamura, H., Rao, A., and Hogan, P.G. (1998). Selective inhibition of NFAT activation by a peptide spanning the calcineurin targeting site of NFAT. Mol. Cell *1*, 627–637.

Beltman, J.B., Marée, A.F.M., and de Boer, R.J. (2009). Analysing immune cell migration. Nat. Rev. Immunol. *9*, 789–798.

Braun, A., Worbs, T., Moschovakis, G.L., Halle, S., Hoffmann, K., Bölter, J., Münk, A., and Förster, R. (2011). Afferent lymph-derived T cells and DCs use different chemokine receptor CCR7-dependent routes for entry into the lymph node and intranodal migration. Nat. Immunol. *12*, 879–887.

Breart, B., Lemaître, F., Celli, S., and Bousso, P. (2008). Two-photon imaging of intratumoral CD8+ T cell cytotoxic activity during adoptive T cell therapy in mice. J. Clin. Invest. *118*, 1390–1397.

Chen, T.W., Wardill, T.J., Sun, Y., Pulver, S.R., Renninger, S.L., Baohan, A., Schreiter, E.R., Kerr, R.A., Orger, M.B., Jayaraman, V., et al. (2013). Ultrasensitive fluorescent proteins for imaging neuronal activity. Nature *499*, 295–300.

Cockburn, I.A., Amino, R., Kelemen, R.K., Kuo, S.C., Tse, S.W., Radtke, A., Mac-Daniel, L., Ganusov, V.V., Zavala, F., and Ménard, R. (2013). In vivo imaging of CD8+ T cell-mediated elimination of malaria liver stages. Proc. Natl. Acad. Sci. USA *110*, 9090–9095.

Deguine, J., and Bousso, P. (2013). Dynamics of NK cell interactions in vivo. Immunol. Rev. *251*, 154–159.

Dustin, M.L. (2008). T-cell activation through immunological synapses and kinapses. Immunol. Rev. *221*, 77–89.

Elemans, M., Seich Al Basatena, N.-K., and Asquith, B. (2012). The efficiency of the human CD8+ T cell response: how should we quantify it, what determines it, and does it matter? PLoS Comput. Biol. *8*, e1002381.

Elemans, M., Florins, A., Willems, L., and Asquith, B. (2014). Rates of CTL killing in persistent viral infection in vivo. PLoS Comput. Biol. *10*, e1003534.

Ganusov, V.V., and De Boer, R.J. (2008). Estimating in vivo death rates of targets due to CD8 T-cell-mediated killing. J. Virol. *82*, 11749–11757.

Garcia, V., Richter, K., Graw, F., Oxenius, A., and Regoes, R.R. (2015). Estimating the In Vivo Killing Efficacy of Cytotoxic T Lymphocytes across Different Peptide-MHC Complex Densities. PLoS Comput. Biol. *11*, e1004178.

Germain, R.N., Robey, E.A., and Cahalan, M.D. (2012). A decade of imaging cellular motility and interaction dynamics in the immune system. Science *336*, 1676–1681.

Gold, M.C., Munks, M.W., Wagner, M., McMahon, C.W., Kelly, A., Kavanagh, D.G., Slifka, M.K., Koszinowski, U.H., Raulet, D.H., and Hill, A.B. (2004). Murine cytomegalovirus interference with antigen presentation has little effect on the size or the effector memory phenotype of the CD8 T cell response. J. Immunol. *172*, 6944–6953.

Halle, S., Dujardin, H.C., Bakocevic, N., Fleige, H., Danzer, H., Willenzon, S., Suezer, Y., Hämmerling, G., Garbi, N., Sutter, G., et al. (2009). Induced bronchus-associated lymphoid tissue serves as a general priming site for T cells and is maintained by dendritic cells. J. Exp. Med. *206*, 2593–2601.

Hansen, S.G., Powers, C.J., Richards, R., Ventura, A.B., Ford, J.C., Siess, D., Axthelm, M.K., Nelson, J.A., Jarvis, M.A., Picker, L.J., and Früh, K. (2010). Evasion of CD8+ T cells is critical for superinfection by cytomegalovirus. Science *328*, 102–106.

Hickman, H.D., Reynoso, G.V., Ngudiankama, B.F., Rubin, E.J., Magadán, J.G., Cush, S.S., Gibbs, J., Molon, B., Bronte, V., Bennink, J.R., and Yewdell, J.W. (2013). Anatomically restricted synergistic antiviral activities of innate and adaptive immune cells in the skin. Cell Host Microbe *13*, 155–168.

Hickman, H.D., Reynoso, G.V., Ngudiankama, B.F., Cush, S.S., Gibbs, J., Bennink, J.R., and Yewdell, J.W. (2015). CXCR3 chemokine receptor enables local CD8(+) T cell migration for the destruction of virus-infected cells. Immunity *42*, 524–537.

Hogan, T., Kadolsky, U., Tung, S., Seddon, B., and Yates, A. (2014). Spatial heterogeneity and peptide availability determine CTL killing efficiency in vivo. PLoS Comput. Biol. *10*, e1003805.

Jenkins, M.R., Mintern, J., La Gruta, N.L., Kedzierska, K., Doherty, P.C., and Turner, S.J. (2008). Cell cycle-related acquisition of cytotoxic mediators defines the progressive differentiation to effector status for virus-specific CD8+ T cells. J. Immunol. *181*, 3818–3822.

Kastenmüller, W., Brandes, M., Wang, Z., Herz, J., Egen, J.G., and Germain, R.N. (2013). Peripheral prepositioning and local CXCL9 chemokine-mediated guidance orchestrate rapid memory CD8+ T cell responses in the lymph node. Immunity *38*, 502–513.

Keefe, D., Shi, L., Feske, S., Massol, R., Navarro, F., Kirchhausen, T., and Lieberman, J. (2005). Perforin triggers a plasma membrane-repair response that facilitates CTL induction of apoptosis. Immunity *23*, 249–262.

Kremer, M., Volz, A., Kreijtz, J.H., Fux, R., Lehmann, M.H., and Sutter, G. (2012). Easy and efficient protocols for working with recombinant vaccinia virus MVA. Methods Mol. Biol. *890*, 59–92.

Krmpotic, A., Messerle, M., Crnkovic-Mertens, I., Polic, B., Jonjic, S., and Koszinowski, U.H. (1999). The immunoevasive function encoded by the mouse cytomegalovirus gene m152 protects the virus against T cell control in vivo. J. Exp. Med. *190*, 1285–1296.

Liu, D., Bryceson, Y.T., Meckel, T., Vasiliver-Shamis, G., Dustin, M.L., and Long, E.O. (2009). Integrin-dependent organization and bidirectional vesicular traffic at cytotoxic immune synapses. Immunity *31*, 99–109.

Lopez, J.A., Brennan, A.J., Whisstock, J.C., Voskoboinik, I., and Trapani, J.A. (2012). Protecting a serial killer: pathways for perforin trafficking and self-defence ensure sequential target cell death. Trends Immunol. *33*, 406–412.

Marangoni, F., Murooka, T.T., Manzo, T., Kim, E.Y., Carrizosa, E., Elpek, N.M., and Mempel, T.R. (2013). The transcription factor NFAT exhibits signal memory during serial T cell interactions with antigen-presenting cells. Immunity *38*, 237–249.

Marchingo, J.M., Kan, A., Sutherland, R.M., Duffy, K.R., Wellard, C.J., Belz, G.T., Lew, A.M., Dowling, M.R., Heinzel, S., and Hodgkin, P.D. (2014). T cell signaling. Antigen affinity, costimulation, and cytokine inputs sum linearly to amplify T cell expansion. Science *346*, 1123–1127.

Marquardt, A., Halle, S., Seckert, C.K., Lemmermann, N.A., Veres, T.Z., Braun, A., Maus, U.A., Förster, R., Reddehase, M.J., Messerle, M., and Busche, A. (2011). Single cell detection of latent cytomegalovirus reactivation in host tissue. J. Gen. Virol. *92*, 1279–1291.

Mempel, T.R., Henrickson, S.E., and Von Andrian, U.H. (2004). T-cell priming by dendritic cells in lymph nodes occurs in three distinct phases. Nature *427*, 154–159.

Mempel, T.R., Pittet, M.J., Khazaie, K., Weninger, W., Weissleder, R., von Boehmer, H., and von Andrian, U.H. (2006). Regulatory T cells reversibly suppress cytotoxic T cell function independent of effector differentiation. Immunity *25*, 129–141.

Newell, E.W., Sigal, N., Bendall, S.C., Nolan, G.P., and Davis, M.M. (2012). Cytometry by time-of-flight shows combinatorial cytokine expression and virus-specific cell niches within a continuum of CD8+ T cell phenotypes. Immunity *36*, 142–152.

Plotkin, S.A. (2013). Complex correlates of protection after vaccination. Clin. Infect. Dis. *56*, 1458–1465.

Regoes, R.R., Yates, A., and Antia, R. (2007). Mathematical models of cytotoxic T-lymphocyte killing. Immunol. Cell Biol. *85*, 274–279.

Ritter, A.T., Asano, Y., Stinchcombe, J.C., Dieckmann, N.M., Chen, B.C., Gawden-Bone, C., van Engelenburg, S., Legant, W., Gao, L., Davidson, M.W., et al. (2015). Actin depletion initiates events leading to granule secretion at the immunological synapse. Immunity *42*, 864–876.

Thiery, J., Keefe, D., Boulant, S., Boucrot, E., Walch, M., Martinvalet, D., Goping, I.S., Bleackley, R.C., Kirchhausen, T., and Lieberman, J. (2011). Perforin pores in the endosomal membrane trigger the release of endocytosed granzyme B into the cytosol of target cells. Nat. Immunol. *12*, 770–777.

Varadarajan, N., Julg, B., Yamanaka, Y.J., Chen, H., Ogunniyi, A.O., McAndrew, E., Porter, L.C., Piechocka-Trocha, A., Hill, B.J., Douek, D.C., et al. (2011). A high-throughput single-cell analysis of human CD8$^+$ T cell functions reveals discordance for cytokine secretion and cytolysis. J. Clin. Invest. *121*, 4322–4331.

West, E.E., Youngblood, B., Tan, W.G., Jin, H.-T., Araki, K., Alexe, G., Konieczny, B.T., Calpe, S., Freeman, G.J., Terhorst, C., et al. (2011). Tight regulation of memory CD8(+) T cells limits their effectiveness during sustained high viral load. Immunity *35*, 285–298.

Wiedemann, A., Depoil, D., Faroudi, M., and Valitutti, S. (2006). Cytotoxic T lymphocytes kill multiple targets simultaneously via spatiotemporal uncoupling of lytic and stimulatory synapses. Proc. Natl. Acad. Sci. USA *103*, 10985–10990.

Yewdell, J.W. (2010). Designing CD8+ T cell vaccines: it's not rocket science (yet). Curr. Opin. Immunol. *22*, 402–410.

Zhang, N., and Bevan, M.J. (2011). CD8(+) T cells: foot soldiers of the immune system. Immunity *35*, 161–168.

Ziegler, H., Thale, R., Lucin, P., Muranyi, W., Flohr, T., Hengel, H., Farrell, H., Rawlinson, W., and Koszinowski, U.H. (1997). A mouse cytomegalovirus glycoprotein retains MHC class I complexes in the ERGIC/cis-Golgi compartments. Immunity *6*, 57–66.

Immunity, Volume *44*

Supplemental Information

In Vivo Killing Capacity of Cytotoxic T Cells Is Limited and Involves Dynamic Interactions and T Cell Cooperativity

Stephan Halle, Kirsten Anja Keyser, Felix Rolf Stahl, Andreas Busche, Anja Marquardt, Xiang Zheng, Melanie Galla, Vigo Heissmeyer, Katrin Heller, Jasmin Boelter, Karen Wagner, Yvonne Bischoff, Rieke Martens, Asolina Braun, Kathrin Werth, Alexey Uvarovskii, Harald Kempf, Michael Meyer-Hermann, Ramon Arens, Melanie Kremer, Gerd Sutter, Martin Messerle, and Reinhold Förster

Figure S1

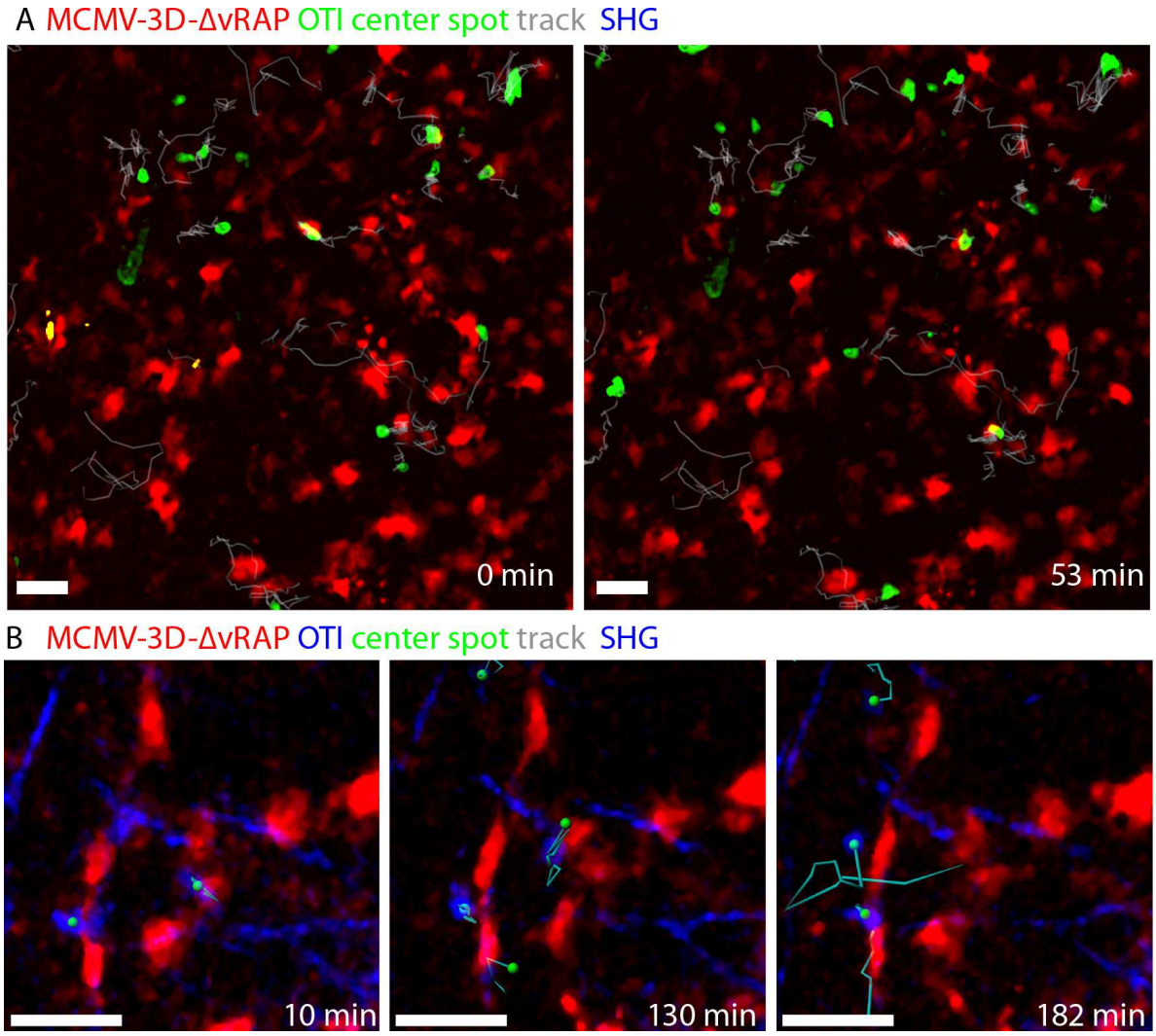

Figure S1, related to Figure 3. Virus-infected cells are not disrupted within minutes when only few virus-specific CTLs are present at the site of infection. (**A**) MCMV-3D-ΔvRAP-infected cells (red) were observed during imaging in regions with few OT-I CTLs (green) present (elapsed time in minutes). (**B**) In a movie with few CFP-OT-I CTLs (blue), virus-infected cells were followed over three hours (green center spots of tracked cells; gray tracks; SHG, blue; Movie S1). Scale bars, 30 µm. CTL were primed with SIINFEKL and poly(I:C). Pictures shown in A and B are derived from Movie S1.

Figure S2

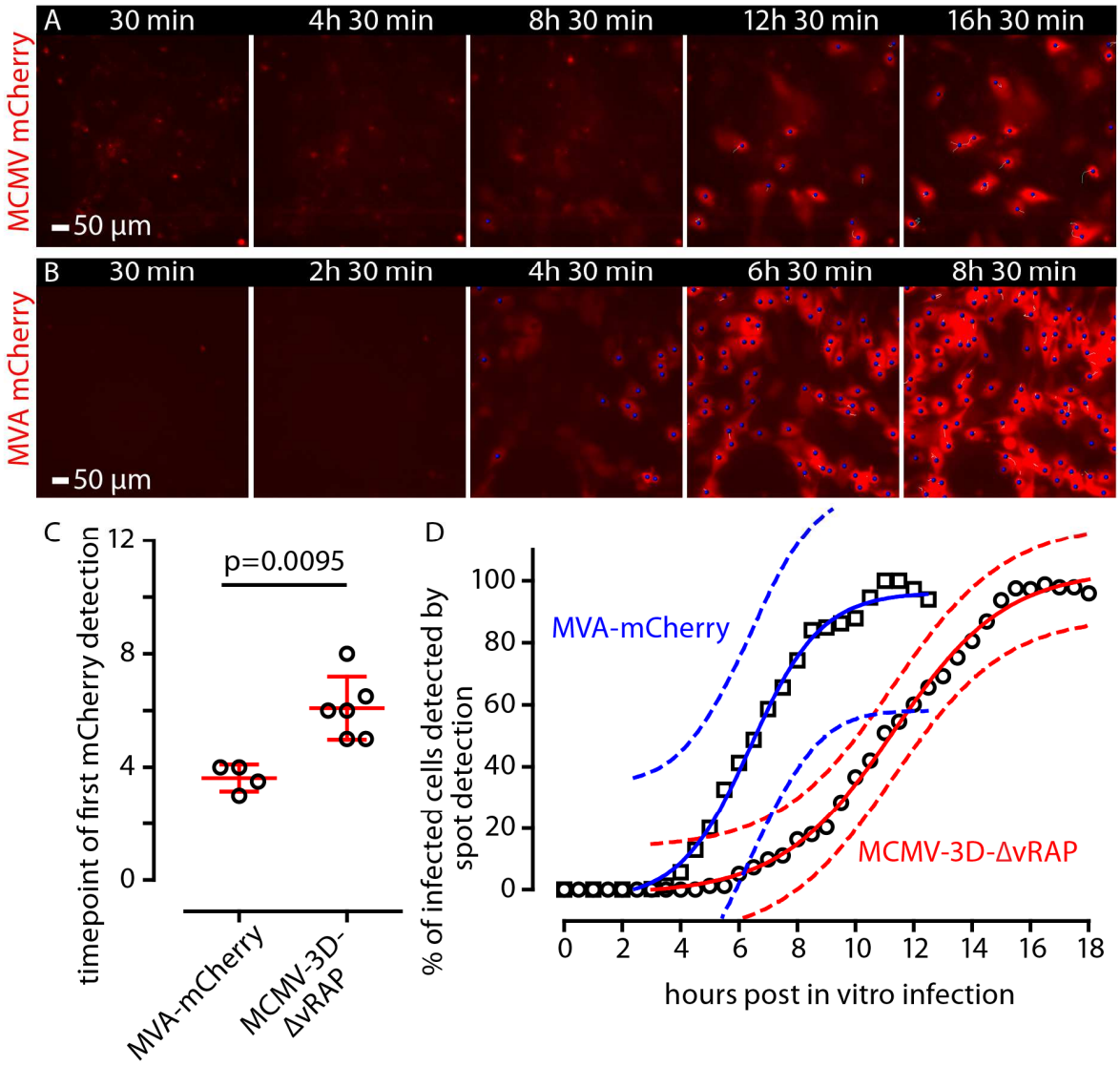

Figure S2, related to Figure 4. Time-lapse microscopy reveals early expression of virus-encoded mCherry. (**A**) C57BL/6 mouse stromal cells were infected *in vitro* with MCMV-3D-ΔvRAP at a MOI of 5-10 (A) or MVA-mCherry at a MOI of 5-10 (**B**). Single cell mCherry fluorescence intensities were monitored by time-lapse live cell microscopy between 30 minutes to 16 hours after infection. Scale bars, 50 µm. Blue spots, automatic detection of infected cells. (**C**) Time of first mCherry detection for the viruses indicated. Dots, movies; lines, mean and standard deviation; p-value, Mann-Whitney test. (**D**) Automated spot detection was used to track mCherry-expressing cells over time. The percentage of the number of detectable cells was plotted over time. Data pooled from 4 experiments; line, sigmoidal dose response curve fitted; dotted lines, 95% prediction interval for the viruses indicated. Pictures shown in A and B are derived from Movie S4.

Figure S3

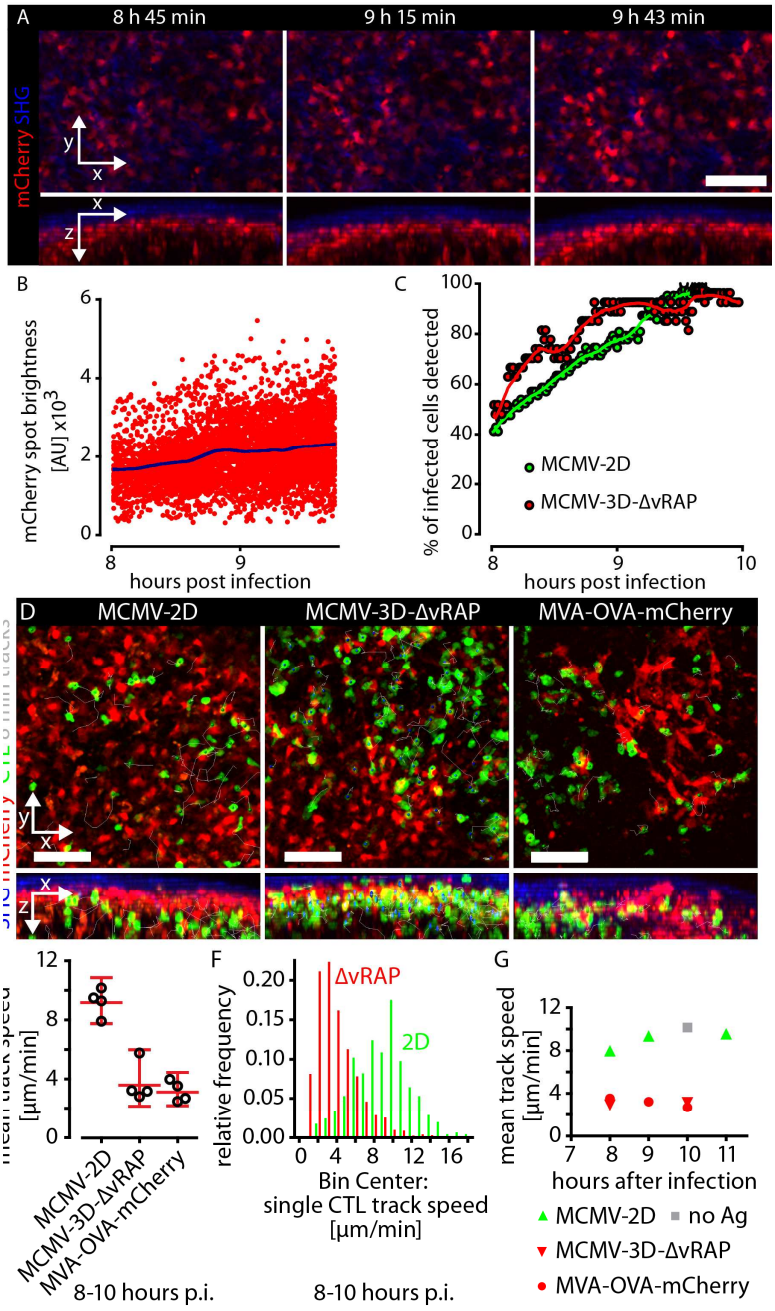

Figure S3, related to Figure 4. SIINFEKL and mCherry are both expressed early after virus infection. (**A**) Mouse popliteal lymph nodes were explanted 8 hours after virus injection into the footpad. Lymph node collagen fibers (blue, SHG) and virus-expressed mCherry (red) were detected by 2-photon microscopy at regular laser intensity. Scale bar, 50 µm. x-z views are shown to control for tissue drift during imaging. (**B**) All mCherry$^+$ cell spots were automatically detected and the mCherry brightness was plotted over time. Blue line, locally weighted scatter-plot smoothing curve. (**C**) For both MCMV-2D and MCMV-3D-ΔvRAP-infected lymph nodes, mCherry-intensity was plotted for the time points indicated after infection. Data shown are representative of 4 independent experiments. Line, locally weighted scatter-plot smoothing curve. (**D**) At 8-10 hours after infection with the viruses indicated, GFP-expressing OT-I CTLs were observed at the site of infection in case the viruses encode the SIINFEKL epitope (middle and right panel). Compared to the images depicted in Figure S2, stronger contrast setting were used here for the mCherry channel. Pictures are representative of 5 independent 2-photon imaging experiments. Scale bars, 50 µm. (**E**) CTL track speed at the site of infection plotted for the three viruses shown in panel (D). (**F**) At 8-10 hours after infection with the indicated viruses, single CTL track speed data frequency distribution is shown from all analyzed CTLs. (**G**) CTL population track speed was analyzed at the time points indicated. Dots, mean values per time-point. Data pooled from 5 independent experiments. CTLs were primed with MVA-OVA.

Figure S4

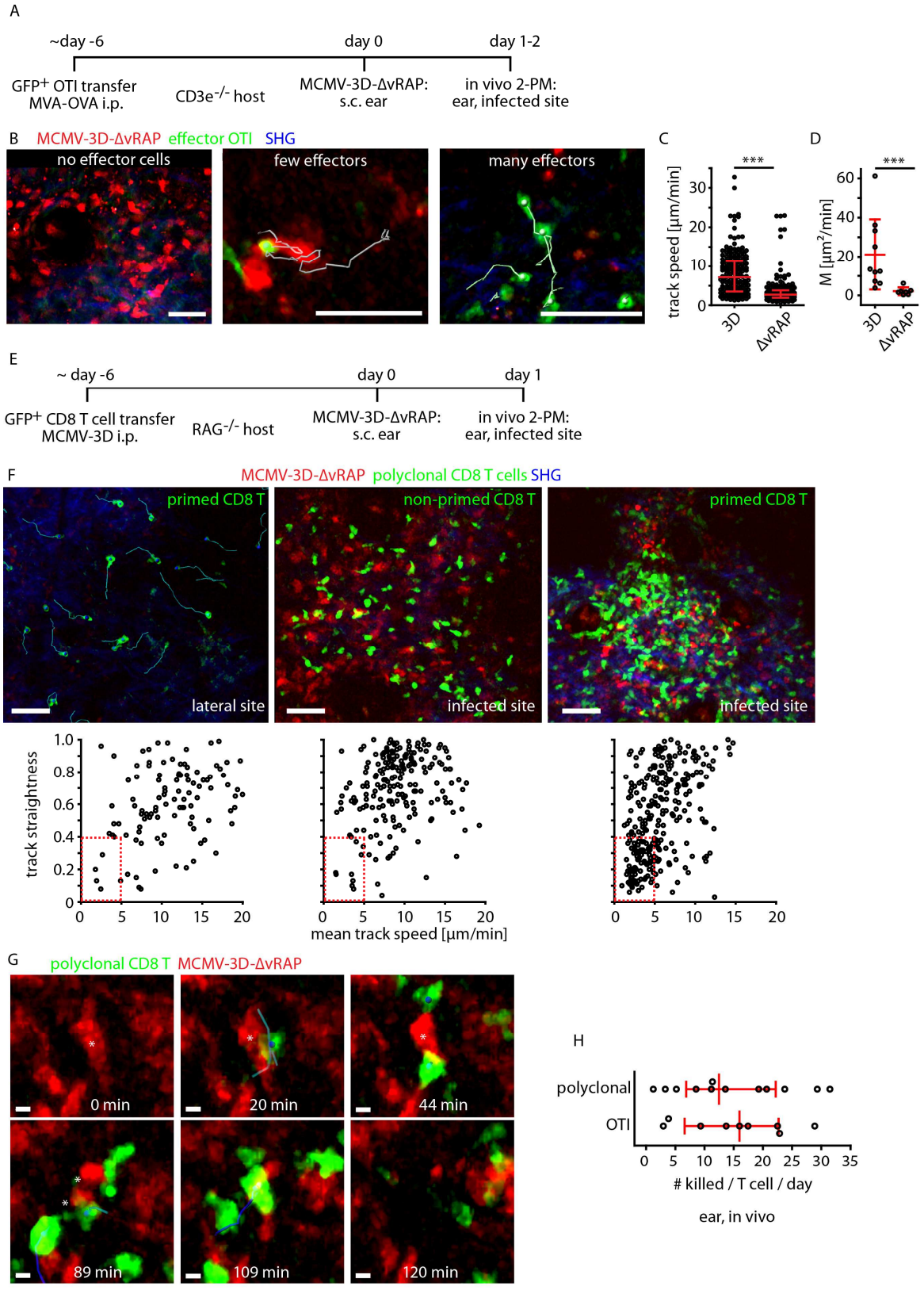

Figure S4, related to Figure 4. *In vivo* imaging of CTLs and MCMV-infected cells in the skin reveals low killing rates. (**A**) Protocol for intravital imaging of OT-I CTL in *Cd3ε*-deficient mice: GFP-expressing naïve OT-I were transferred and MVA-OVA was used to prime the SIINFEKL-specific antiviral response. (**B**) Following MCMV-3D-ΔvRAP infection in the ear, intravital imaging was used to visualize the infected cells in mice without CTLs (left), with few CTLs (middle) or many CTLs (right). OT-I CTL track speed (**C**) and motility coefficient (**D**) was analyzed during interaction of CTLs and infected cells. Dots, cells (C) and movies (D). Data pooled from 3 experiments; Mann-Whitney test. Scale bars, 20 µm. (**E**) Protocol for intravital imaging of *Rag2*$^{-/-}$

mice reconstituted with polyclonal FP-CD8$^+$ T cells and primed (MCMV-3D i.p.) or not primed six to seven days earlier. (**F**) Migratory behavior of FP-CTLs cells one day after secondary ear infection with MCMV-3D-ΔvRAP at conditions indicated. The percentage of cells in the boxed region was used as the percentage of MCMV-specific CTLs (lower panel: dots, cells; data from 1-4 movies collected in 6 independent experiments). (**G**) Polyclonal FP-CTLs contacted infected cells. Asterisks point to target disruption. (**H**) *In vivo* per capita killing rate of polyclonal or OT-I CTLs in the ear skin determined by intravital microscopy (dots, movies; pooled from 2 to 4 independent experiments). Scale bars, 50 µm (F) or 5 µm (G). Data shown in F and G are taken from Movie S5.

Figure S5

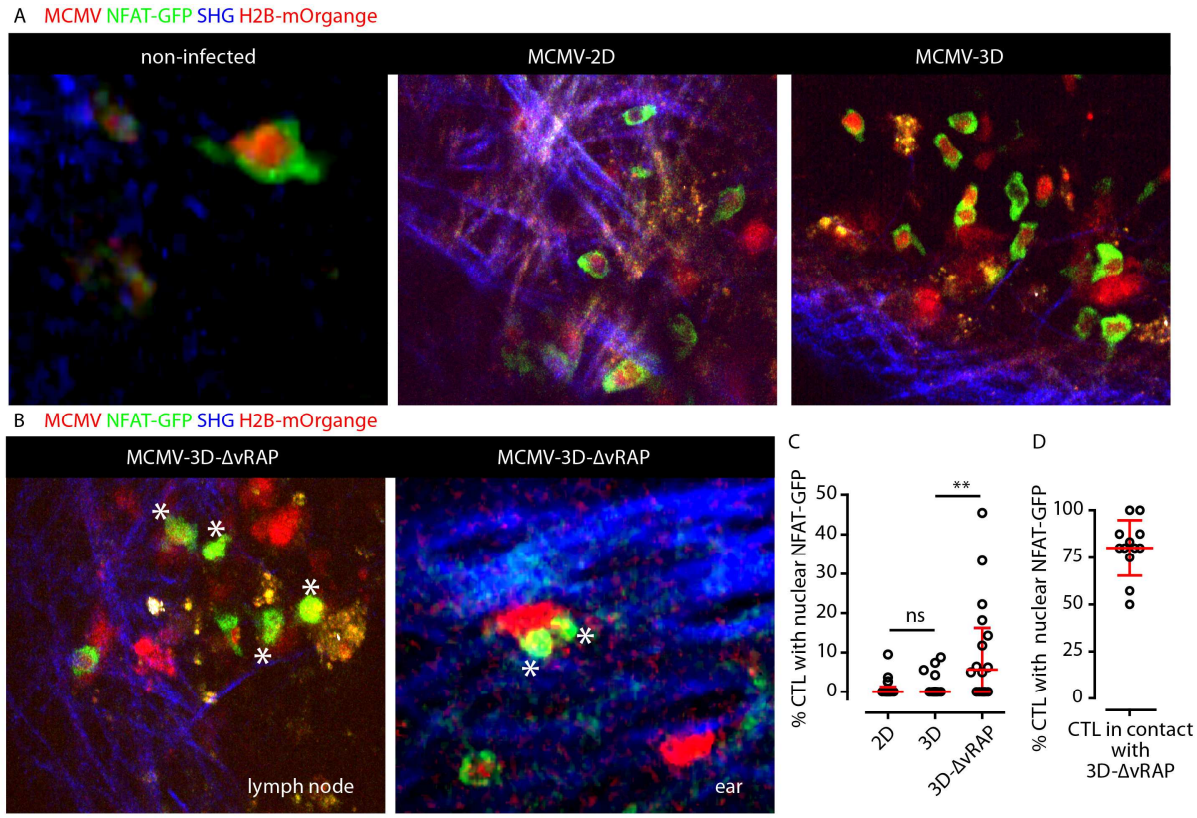

Figure S5, related to Figure 7. Viral immune evasion prevents NFAT signaling in virus-specific CTLs. NFAT-GFP and H2B-mOrange-expressing naïve OT-I CD8$^+$ T cells were transferred into mice followed by T cell priming and expansion by treatment with MVA-OVA. One week later, NFAT-GFP (green) and H2B-mOrange (red) CTLs were observed by 2-photon microscopy in non-infected lymph nodes, MCMV-2D or MCMV-3D-infected lymph nodes. (**A**) NFAT-OT-I CTLs showed a cytoplasmatic GFP signal that spared the mOrange$^+$ nucleus in lymph nodes infected with MCMV-2D or MCMV-3D. (**B**) In lymph nodes or ear dermis infected with MCMV-3D-ΔvRAP, NFAT-OT-I CTLs in contact with target cells showed a nuclear NFAT-GFP signal. (**C**) The percentage of NFAT-OT-I CTLs with a nuclear NFAT-GFP signal was analyzed for lymph nodes infected with MCMV-2D, MCMV-3D or MCMV-3D-ΔvRAP (dots, movies; data pooled from 19 lymph nodes from 3 independent experiments). (**D**) For the CTLs in contact with MCMV-3D-ΔvRAP-infected cells, the percentage of nuclear NFAT-GFP was analyzed (percentage of all CTLs in contact with MCMV-3D-ΔvRAP-infected cells; dots, movies; data pooled from 5 independent experiments). See also Movie S6.

Figure S6

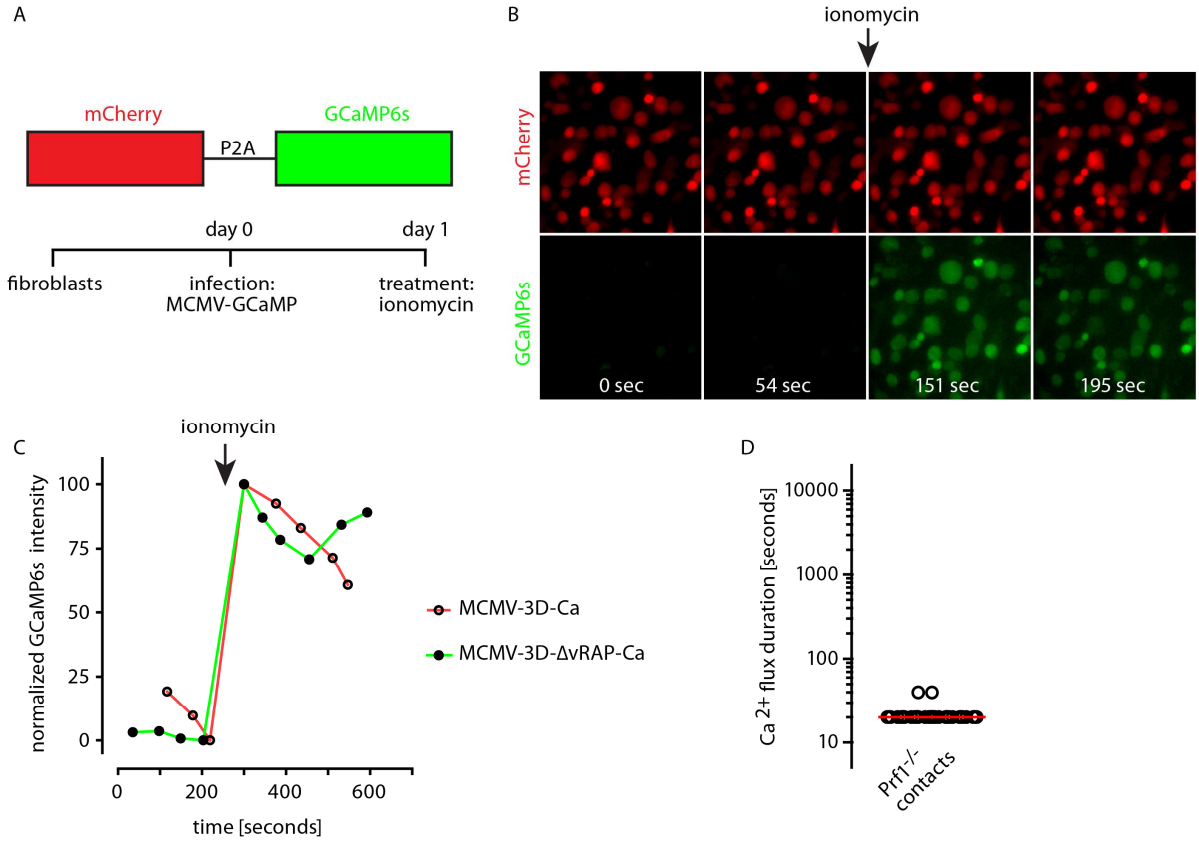

Figure S6, related to Figure 7. Viral expression of GCaMP6s allows for visualization of Ca^{2+}-signaling in virus-infected cells. (**A**) Mouse fibroblasts were infected *in vitro with* the MCMV-strains expressing mCherry and the GCaMP6s Ca^{2+}-sensor and treated with ionomycin. (**B**) *In vitro*, very low GCaMP6s-fluorescence (green) was observed before ionomycin treatment. Some infected cells showed spontaneous Ca^{2+} signals. Following ionomycin addition, all mCherry-expressing cells (red) showed a prolonged green fluorescent signal (observed in 4 experiments). (**C**) Normalized GCaMP6s-fluorescene intensity before and after ionomycin treatment *in vitro* (data pooled from 2 independent experiments). (**D**) Perforin-deficient CTLs were intra-lymphatically transferred and contact events with MCMV-3D-ΔvRAP-Ca-infected cells were analyzed (dots, flux events; 68 events analyzed in total, data pooled from 3 experiments with explanted lymph nodes). See also Movie S7.

Figure S7

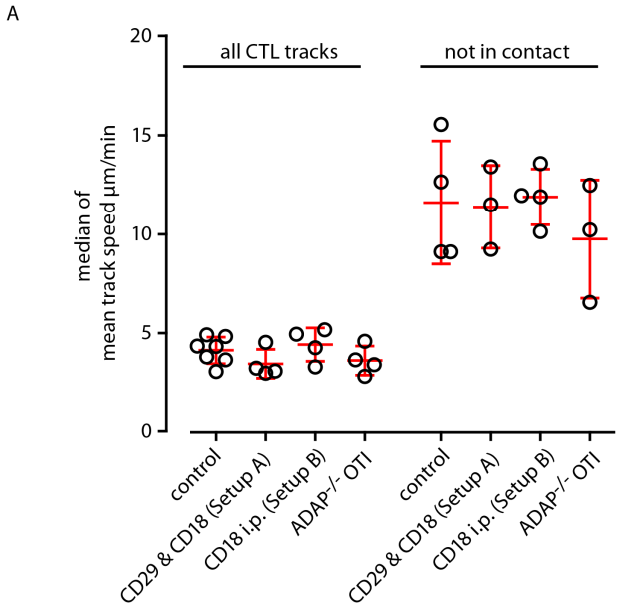

Figure S7, related to Figure 7. Virus-specific CTLs migrate slowly during attack on virus-infected cells independently of ADAP or integrin function. (**A**) Virus-specific OT-I CTLs "scanning" migration was analyzed after blockade of beta-1 and beta-2 integrins. CTL track speed was analyzed during attack on MCMV-3D-ΔvRAP-infected cells in the virus-infected region of the popliteal lymph node on one day after virus infection (all CTL tracks). Intra-lympatic transfer of non-treated (control group) or anti-CD29 and anti-CD18 treated CTLs (setup A) was performed. In setup B, the recipient mouse was treated with an intra-peritoneal injection of 400 µg of anti-CD18 antibody prior to CTL transfer. Data pooled form 4 independent experiments. *Adap*$^{-/-}$ OT-I CTLs were injected in two independent experiments. Explanted lymph nodes were imaged. CTLs were primed by MVA-OVA. All CTLs were tracked to allow direct comparison between groups (left; marked as "all CTL tracks"). To test whether CTLs that freely migrate and that are not in contact with virus-infected cells show the normal track speed of around 10 µm/min, these cells were identified and re-analyzed separately (right; marked as "not in contact"). Dots, median values of all CTLs per movie; Lines, mean; error bars, standard deviation; Kruskal-Wallis test p-value = 0.24 (all CTL tracks) and 0.82 (not in contact).

Supplemental Experimental Procedures

Murine cytomegalovirus (MCMV) strains: All MCMV strains were derived from BAC pSM3fr cloned Smith strain, as described previously (Marquardt et al., 2011). Notably, all MCMV strains used in this study do not express m157, which is a natural killer cell-activating viral protein in B6 mice. MCMV stocks were generated by ultracentrifugation through a sucrose cushion and titrated on murine fibroblasts, yielding comparable plaque-forming units (PFU) per ml stock across all virus preparations used. The MCMV-3D-Ca and MCMV-3D-ΔvRAP-Ca BACs were derived from the MCMV-3D and MCMV-3D-ΔvRAP BACs (Marquardt et al., 2011), employing the *en passant* mutagenesis protocol (Tischer et al., 2010). Briefly, a kanamycin resistance (KanR) cassette (including an I-SceI site and a sequence duplication required for subsequent deletion of KanR) was inserted at the 3'-end of the ORF of the Ca^{2+}-binding protein calmodulin (CaM) in plasmid pGP-CMV-GCaMP6s (Chen et al., 2013) obtained from Addgene (plasmid #40753). The CaMP6s-KanR cassette was amplified using primers with homologies to the P2A and SV40p(A) signal sequences present within the MCMV-3D and MCMV-3D-ΔvRAP BACs. PCR products were transfected into *E. coli* GS1783 cells containing either one of the respective BACs and the KanR cassette was excised after successful insertion.

Modified Vaccinia virus Ankara (MVA) strains: Recombinant MVA-OVA viruses have been described previously (Halle et al., 2009; Lehmann et al., 2009). MVA-mCherry and MVA-OVA-mCherry were generated by homologous recombination using the plasmid vectors pIIIdHR-P7.5 and pLW-73 according to standard procedures (Kremer et al., 2012). The mCherry coding sequence was inserted in the I8R/G1L intergenic site, under transcriptional control of the vaccinia virus-specific synthetic early-late promoter PmH5. The ovalbumin gene was placed at the site of deletion III in the MVA genome and expressed by the natural viral early-late promoter P7.5. All MVA viruses were amplified and titrated on primary chicken embryonic fibroblasts. High titer MVA stocks were obtained by ultracentrifugation through sucrose and stored in 1 mM Tris-HCl pH 9.0 at -80°C.

Mouse infection models: Mice were anaesthetized by intraperitoneal (i.p.) injection of ketamine (100 mg/kg) and xylazine (5 mg/kg) and subsequently injected subcutaneously (s.c.) into the hind footpad (or the ear) with 10^6 PFU of the different MCMV strains diluted in 25-50 µl phosphate buffered saline (PBS). For MVA infections, 10^7 PFU of virus were diluted in 25-50 µl PBS and injected s.c. into the hind footpad. The time of virus injection was defined as time of infection.

Generation of OT-I CTLs *in vivo*: Lymphocytes from CD45.1$^+$ FP-OT-I mice, containing 10^5 CD8$^+$ TCR Vα5$^+$ OT-I cells, were injected i.p. or i.v. into recipient male C57BL/6, into *Cd3ε*-deficient or perforin-deficient mice. One day later, FP-OT-I cells were activated *in vivo* by vaccination with 17 µg SIINFEKL-peptide injected i.p., together with 85 µg poly(I:C) (Sigma). Alternatively, s.c. footpad injection of 50 µg OVA-protein (Sigma) together with MVA-wt as an adjuvant, or SIINFEKL peptide plus incomplete Freund's adjuvant (IFA, Sigma), was used to generate effector FP-OT-I cells. In some experiments, *Cd3ε*$^{-/-}$ mice that lack any endogenous T cells were used as recipients in combination with 10^4-10^5 FP-OT-I transferred before MVA-OVA i.p. priming with 1-5x10^6 PFU per mouse.

Generation of MCMV-specific CTLs from the endogenous repertoire: To generate MCMV-specific CTLs, naïve GFP- or CFP-expressing B6 mice were i.p. infected with 10^6 PFU MCMV-3D, and lymphoid organs were harvested 6 - 8 days later. Next, CD8$^+$ T cells were enriched by negative selection (MACS). Subsequently, 2 – 5 x10^6 CD8$^+$ T cells were stained with M45$_{985\text{-}993}$ D^b tetramer (Munks et al., 2006) and positively selected using anti-biotin magnetic beads. Approximately 60% of selected cells were CD8$^+$CD44$^+$ M45-labelled CTLs. MHC-I tetramers were prepared as described (Altman et al., 1996). Alternatively, bulk effector CD8$^+$ T cells (poly-specific for different MCMV-epitopes) were labeled with TAMRA or CMFDA (CellTracker green, Thermo Fisher Scientific) and enriched for effector cells by depleting CD62L^{hi} naïve CD8$^+$ T cells by MACS, yielding 60-70% CD8$^+$ CD44^{hi} T cells. For FACS sorting, M45-, M38- and m139-tetramer-binding CD8$^+$ T cells were selected from MACS-purified CD8$^+$ T cells, yielding 90% CD8$^+$CD44$^+$tetramer$^+$ CTLs used for CMFDA-labelling and intra-lymphatic delivery. For intravital imaging, CD8$^+$ MACS-purified GFP-B6 cells were transferred into *Rag2*-deficient mice, followed by i.p. primary infection with 10^6 PFU MCMV-3D.

Cell culture: Human 293T and murine SC-1 cells were grown in High-glucose [4.5 g/L] Dulbecco's modified Eagles medium including stable glutamine (DMEM; Biochrom, Berlin, Germany) supplemented with 10% (v/v) fetal calf serum (FCS), 1 mM sodium pyruvate and 1% (v/v) Penicillin/Streptomycin (all PAA, Coelbe, Germany).

Cloning of the NFAT-GFP construct: Plasmids pRSF91.NFATeGFP.PRE*, encoding a fusion protein of amino acids 1-460 of mouse NFAT1 and eGFP, as well as pRSF91.synH2BmOrange.PRE* are derived from the gammaretroviral vector plasmid pRSF91.eGFP.PRE*. NFATeGFP (Aramburu et al., 1998) was introduced into

pRSF91.eGFP.PRE* by ligating the 957 bp (NcoI / BamHI) and 1152 bp (BamHI / BsrgI) fragments of pMSCV.NFATeGFP.Puro with the 4918 bp back bone fragment (NcoI / BsrgI) of pRSF91.eGFP.PRE*. To facilitate cloning of pRSF91.synH2BmOrange.PRE* we used gene synthesis (Integrated DNA Technologies, Leuven, Belgium) to introduce restriction sites Acc65I and AgeI upstream of the ATG start codon and to eliminate restriction sites BsrgI, BspmI and AgeI within the first 430 bp of H2B without changing the amino acid code. The synthesized product synH2B was introduced into pCDNA3.H2BmOrange (Addgene plasmid 20969, (Nam and Benezra, 2009) by ligating the 5388 bp (XbaI / Acc65I) and 681 bp (MscI / XbaI) fragments of pCDNA3.H2BmOrange with synH2B (Acc65I / MscI) resulting in plasmid pCDNA3.synH2BmOrange. Finally, the EGFP expression cassette of pRSF91.EGFP.PRE* was replaced by synH2BmOrange using restriction enzymes AgeI and BsrgI.

Gammaretroviral particles and generation of NFAT-GFP OT-I T cells: Gammaretroviral particles were produced as previously described (Galla et al., 2013). In brief, $5x10^6$ 293T cells were seeded in surface-treated 10 cm-culture dishes. The next day, cells were transfected with 5 µg pRSF91.NFATeGFP.PRE* or pRSF91.H2BmOrange.PRE* together with 7 µg pCDNA3.MLV.Gag/Pol and 3 µg pEnv(eco)-IRES-puro expression plasmids (kindly provided by T. Kitamura, Japan (Morita et al., 2000)) using the Ca^{2+} phosphate transfection method assisted by 25 µM chloroquine (Sigma Aldrich). Gammaretroviral supernatants were harvested 36 and 60 h post-transfection, filtered through a 0.22 µm filter (Millipore), pooled and overnight 50x concentrated via ultracentrifugation at 13,238 x g and 4°C. Gammaretroviral vector supernatants were titrated by transducing 1 x 10^5 SC-1 cells with serial dilutions of the concentrated supernatant in the presence of 4 µg / mL protamine sulfate (Sigma Aldrich) and centrifugation for 60 min at 400 x g and 30-37°C. Two days later, cells were analyzed by flow cytometry and the transducing units / mL of each supernatant was determined by using experiments showing transduction efficiencies below 30%. Bone marrow chimeric mice were generated by infecting OT-I mouse bone marrow cells with the gammaretroviral vector supernatants and transfer of NFAT-GFP-expressing cells into irradiated C57BL/6 recipients. 6 weeks later, NFAT-GFP expression in OT-I $CD8^+$ T cells was observed in blood cells by flow cytometry and mice showing the brightest NFAT-GFP signal were used as donors of naïve NFAT-GFP OT-I $CD8^+$ T cells.

Intra-lymphatic injection of CTLs: We intra-lymphatically (i.l.) transferred different numbers of CTLs 2 - 6 hours following MCMV-3D-ΔvRAP infection. Injection was performed as described before (Braun et al., 2011). Briefly, 2.5 x 10^4 – 1 x 10^5 CTLs diluted in 5 µl PBS were injected in 90 seconds into the afferent lymph vessel draining towards the popliteal lymph node.

Organ preparation: For histology, tissue was fixed in 2% PFA overnight and embedded in OCT compound (Tissue-Tek). For flow cytometry, single-cell suspensions were prepared by mechanical disruption. Cells were blocked with 5% rat serum, stained and analyzed with a LSRII cytometer (BD Biosciences). Data was analyzed using WinList 6.0 (Verity Software House). The following antibodies were used: CD8-beta-Cy5 (RMCD8-2), CD44-eFluor 450 (IM7), CD62L-biotin (MEL-14), CD169-Alexa647 (MOMA-1), CD11b-PE-Cy7 (M1/70), CD11b-PE (M1/70), CD69-PerCP-Cy5.5 (H1.2F3), CD45-APC or FITC (30-F11), CD18 (2E6), CD18 (M18/2), CD29 (Hmβ1-1).

Fluorescence microscopy: Unfixed organs were inspected directly after dissection under fluorescence illumination (Leica Macroscope). PFA-fixed organs were embedded in OCT compound, sections were rehydrated in Tris-buffered saline with 0.05% Tween-20 (Sigma), blocked with 2.5% rat and 2.5% mouse serum and stained at room temperature for 30 minutes. Pictures were taken using a Zeiss Axiovert fluorescence microscope and AxioVision 4.6 software (Carl Zeiss, Germany). All pictures were contrast adjusted. For time-lapse *in vitro* imaging, the microscope imaging chamber was heated to 37°C and cells were cultured in sealed Lab-Tek II chamber slides (Nalge Nunc International, USA) in RPMI medium with 10% FCS, 1% Penicilin-Streptomycin, 1% L-Glutamin and 10 mM Hepes.

2-photon microscopy: Explanted lymph nodes were immobilized in an imaging chamber using tissue adhesive (Surgibond) and superfused with oxygenated (95% O_2 with 5% CO_2) RPMI medium (Invitrogen, Thermo Fisher Scientific) containing 5 g/L D(+) glucose monohydrate (Sigma) as described (Halle et al., 2009). Lymph nodes (LN) were kept shortly at 4°C before imaging at 37.5°C. Explanted lymph nodes were stored for 5-20 min on ice in RPMI 1640. After a 15 min equilibration at 37.5°C, CTLs showed regular migration (not shown). For intravital imaging of the ear, anaesthetized mice were placed on a 37°C warm stage and the imaging region was covered with PBS. The following microscope setup was used for 2-photon imaging: TriM Scope (LaVision BioTec), Olympus BX51 upright microscope, 20× 0.95 NA water immersion objective, two Mai Tai Titanium:sapphire pulsed infrared lasers (Newport Corporation, Spectra-Physics). One Laser was tuned to 920 nm for excitation of GFP, CMFDA, CFP and TAMRA. The second Mai Tai laser was used to drive an optical parametric oscillator (OPO; APE, Berlin) to generate 1100 nm light to excite mCherry. To generate time-lapse series, Z-stacks of up to 10-18 images were acquired every 6 - 60 sec. 400 µm x 400 µm x 80 µm view fields of

the afferent side of the popliteal LNs were acquired. The same imaging region was used throughout this study, defined by the first B cell follicle visible on the cortical LN side, as determined by typical auto-fluorescence and shape. Data analysis of 2-photon imaging was performed using Imaris 7.2-8.0.1 (Bitplane). The presence of intact virus-infected cells was determined by manual inspection of every single infected cell in the single-slice visualization mode of the Imaris software. All movies were median-filtered for noise reduction. When needed, Imaris drift correction was applied. In all movies, the position of all virus-infected cells was checked in 3D over time to exclude loss of target cells by tissue drift. Tracking was done with cell diameters of 5 - 7 µm for T cells and 9-11 µm for virus-infected cells, maximum distance of 6 - 15 µm, gap size of 0 - 5 and manual inspection of tracks. When displayed, tracks are shown as cylinders or lines and center spots indicate the tracked cell at the current position. Real elapsed time is displayed in all movies. To quantify the number of virus-infected cells by 2-photon microscopy, we imaged a 400 µm x 400 µm x 80 µm volume, centered on the virus-infected site below the afferent subcapsular sinus. This imaging volume contained 50 ± 31 and 50 ± 23 (mean ± SD) virus-infected cells one day p.i. with MCMV-3D or MCMV-3D-ΔvRAP, respectively. For analysis of Ca^{2+} flux events, movies were drift corrected and the CTL contact start and end-points were recorded. In parallel, the start and end frames of bright GCaMP6s signals were recorded. A flux event observed to last over 30 seconds was called a "long-lasting" flux event. All long-lasting flux events were analyzed whether they followed a CTL contact and how much time had elapsed between CTL contact initiation and first frame of the bright GCaMP6s-signal. When virus-infected cells were disrupted, the mCherry-labelled remnants often showed a very long-lasting GCaMP6s-signal until the remnants disappeared.

Estimation of single CTL killing capacity from 2-photon movie datasets: To calculate the per capita killing rate (PCKR) of CTLs, we used Imaris spot detection to determine the number of effector cells per imaging volume during the first 10 time-points (the CTL number present at the start remained stable over time). Next, the number of infected cells was recorded at each time-point, yielding the number of infected cells killed. The average number of infected cells killed per CTL in 24 hours, i.e. the per capita killing rate (PKCR), was calculated as follows: $[(T_{start} - T_{end}) / E] \times 24 / t_{movie}$ (T_{start}, number of infected cells at beginning; T_{end}, number of infected cells at end of movie; E, number of effectors cells (mean CTL number from the first 10 time-points); t_{movie}, duration of the movie in hours). Note that the PCKR is normalized to the duration of 24 hours. The mathematical model is based on single-time-point pictures (taken 24 hours after infection and CTL i.l. transfer) and is described in detail below (Mathematical Model).

Analysis of CTL cooperativity: The pooled imaging data was compared against a null hypothesis that does not assume CTL cooperativity, that means, that simply states that the target cell death probability at each CTL contact is an independent event with a level of p(target cell death with single CTL contact)=0.14 (observed probability of target cell death upon single CTL attack). The probability of target cell death was plotted for infected cells that were contacted by zero to fourteen CTL. The p-values were calculated using the one-tailed exact binomial test.

Statistical analysis: Statistical analysis was performed with GraphPad Prism 4. When comparing two groups, p-values were calculated with the nonparametric Mann-Whitney test. To compare multiple groups, the Kruskal-Wallis test was used, in combination with Dunn's test. Error bars represent mean and standard deviation (SD), or median and inter-quartile range (IQR), as indicated. Linear regression analysis was used when a roughly linear relation was observed between two parameters. Non-linear regression analysis was performed fitting a one-phase exponential decay curve to the data. Three outliers are not displayed in Fig.5E, but included in the dataset for the Kruskal-Wallis test. To plot the one-phase exponential decay curve, two outliers (indicated by x) were excluded from regression analysis in Fig.6A. Where applicable, p-values are indicated in the figures as follows: *, $p<0.05$; **, $p<0.01$; ***, $p<0.001$. All experiments shown were performed at least twice. All mice were randomly assigned to treatment groups. Blinded outcome analysis was performed for data shown in Fig.6B and Figure S5C to exclude observer bias in quantification of infected cell numbers or NFAT-GFP scoring, respectively. All experimental data for each figure item are shown, there are no datasets for figure items that were analyzed but not presented.

Mathematical Model: The experimental data consist of the numbers of infected cells that survived after 24 hours in the presence of different T cell numbers following intra-lymphatic CTL transfer. The killing kinetics of T cells was described with a simple rate equation

$$\frac{dI}{dt} = -kTI$$

where I is the number of infected cells, T the number of T cells, and k is the parameter to be estimated. Such a model is based on the assumption that the probability of an infected cell to be killed by a T cell depends only on

the number of T cells, but not on the time. In the process of killing only one T cell participates, so no cooperative behavior was considered in this model. The number of infected cells at the time point *t* is

$$I(t) = I_0\, exp(-kTt)$$

where I_0 is the initial number of infected cells. We assume that cells can die only due to interaction with cognate effector CD8 T cells, since we did not observe any lysis of infected cells in the absence of T cells. The number of T cells is assumed to be constant during the whole experiment. Since there were two different scales of microscopy measurement, 400 µm x 400 µm and 500 µm x 500 µm, we scaled all the numbers to the 400 µm x 400 µm setup. We assume that the initial number of infected cells is log-normally distributed, $\log I_{exp} = \log I_0 - kTt + \epsilon$, where $\epsilon \sim N(0, \sigma)$. Four different killing rates *k* for every experimental condition and I_0 were estimated by multiple linear regression using R (R Core Team, 2015).

We consider zero values as censored measurements and use the substitute method to treat them (G.J. Nehls, 1973). Outliers were detected using robust regression as described in (Motulsky and Brown, 2006). For perforin knockout T cells (*Prf1*$^{-/-}$), which lack any killing activity, *k* is close to zero, and since we did not impose any restriction on it, *k* may become negative (see Fig. M1, below).

The per capita killing rate (PCKR) is defined here as the number of killed cells divided by the T cell number and the time of the experiment:

$$PCKR\ (T,t) = \frac{I(0) - I(t)}{T \times t}$$

where *I(t)* is the number of infected cells at the time point *t*. We did not observe any killing activity during the first 10 hours after injection of T cells. Ignoring this would potentially underestimate the PCKR and *k*. Therefore, we reduce the actual duration of T cell activity correspondingly:

$$PCKR\left(T, \frac{14}{24}[day]\right) = \frac{I(0) - I\left(\frac{14}{24}\ [day]\right)}{T \times \frac{14}{24}\ [day]}$$

The PCKR, in contrast to the parameter *k*, depends on the number of T cells (see Fig. M2, below) and the time of the experiment. Note that *k* is more suitable for comparison of the killing activity of T cells in different experiments. However, for the purpose of illustration, in this study we show PCKRs computed for one T cell and I_0 infected cells obtained from fitting the data from Figure 6A-C. For every experimental condition we calculated the PCKRs based on the estimated values of *k* and estimated its confidence interval using the 95% confidence interval of *k*.

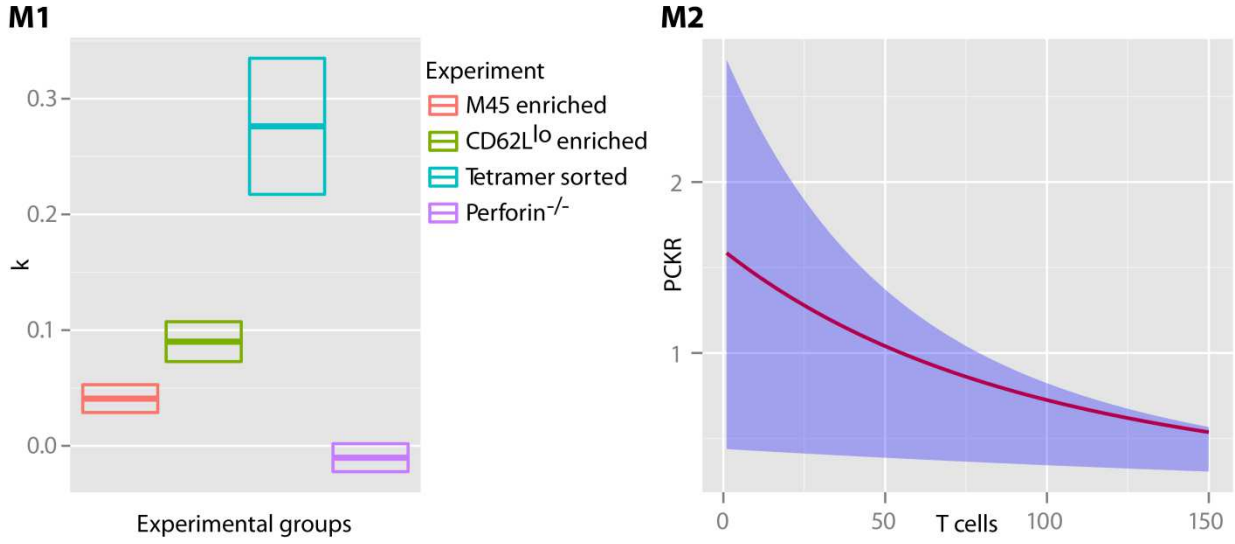

Figure **M1:** Estimations of the parameter k ($[day]^{-1}[cell]^{-1}$) and its 95% confidence interval corresponding to four experimental conditions. Figure **M2**: An example of dependence of PCKR on the number of T cell (M45-enriched). Shaded area corresponds to 95% confidence interval.

Supplemental References

Altman, J. D., Moss, P. A., Goulder, P. J., Barouch, D. H., McHeyzer-Williams, M. G., Bell, J. I., McMichael, A. J., and Davis, M. M. (1996). Phenotypic analysis of antigen-specific T lymphocytes. Science *274*, 94-96.

Aramburu, J., Garcia-Cozar, F., Raghavan, A., Okamura, H., Rao, A., and Hogan, P. G. (1998). Selective inhibition of NFAT activation by a peptide spanning the calcineurin targeting site of NFAT. Mol Cell *1*, 627-637.

Braun, A., Worbs, T., Moschovakis, G. L., Halle, S., Hoffmann, K., Bolter, J., Munk, A., and Forster, R. (2011). Afferent lymph-derived T cells and DCs use different chemokine receptor CCR7-dependent routes for entry into the lymph node and intranodal migration. Nat Immunol *12*, 879-887.

Chen, T. W., Wardill, T. J., Sun, Y., Pulver, S. R., Renninger, S. L., Baohan, A., Schreiter, E. R., Kerr, R. A., Orger, M. B., Jayaraman, V., *et al.* (2013). Ultrasensitive fluorescent proteins for imaging neuronal activity. Nature *499*, 295-300.

G.J. Nehls, G. G. A. (1973). Procedures for handling aerometric data. Journal of the Air Pollution Control Association *23*, 180–184.

Galla, M., Schambach, A., and Baum, C. (2013). Retrovirus-based mRNA transfer for transient cell manipulation. Methods Mol Biol *969*, 139-161.

Halle, S., Dujardin, H. C., Bakocevic, N., Fleige, H., Danzer, H., Willenzon, S., Suezer, Y., Hämmerling, G., Garbi, N., Sutter, G., *et al.* (2009). Induced bronchus-associated lymphoid tissue serves as a general priming site for T cells and is maintained by dendritic cells. J Exp Med *206*, 2593-2601.

Kremer, M., Volz, A., Kreijtz, J. H., Fux, R., Lehmann, M. H., and Sutter, G. (2012). Easy and efficient protocols for working with recombinant vaccinia virus MVA. Methods Mol Biol *890*, 59-92.

Lehmann, M. H., Kastenmuller, W., Kandemir, J. D., Brandt, F., Suezer, Y., and Sutter, G. (2009). Modified vaccinia virus ankara triggers chemotaxis of monocytes and early respiratory immigration of leukocytes by induction of CCL2 expression. J Virol *83*, 2540-2552.

Marquardt, A., Halle, S., Seckert, C. K., Lemmermann, N. A., Veres, T. Z., Braun, A., Maus, U. A., Forster, R., Reddehase, M. J., Messerle, M., and Busche, A. (2011). Single cell detection of latent cytomegalovirus reactivation in host tissue. J Gen Virol *92*, 1279-1291.

Morita, S., Kojima, T., and Kitamura, T. (2000). Plat-E: an efficient and stable system for transient packaging of retroviruses. Gene Ther *7*, 1063-1066.

Motulsky, H. J., and Brown, R. E. (2006). Detecting outliers when fitting data with nonlinear regression - a new method based on robust nonlinear regression and the false discovery rate. BMC Bioinformatics *7*, 123.

Munks, M. W., Gold, M. C., Zajac, A. L., Doom, C. M., Morello, C. S., Spector, D. H., and Hill, A. B. (2006). Genome-wide analysis reveals a highly diverse CD8 T cell response to murine cytomegalovirus. J immunol *176*, 3760-3766.

Nam, H. S., and Benezra, R. (2009). High levels of Id1 expression define B1 type adult neural stem cells. Cell Stem Cell *5*, 515-526.

R Core Team (2015). R: A Language and Environment for Statistical Computing.
Tischer, B. K., Smith, G. A., and Osterrieder, N. (2010). En passant mutagenesis: a two step markerless red recombination system. Methods Mol Biol *634*, 421-430.